The Milky Way Tomography with SDSS: II. Stellar Metallicity

Željko Ivezić[1], Branimir Sesar[1], Mario Jurić[2], Nicholas Bond[3], Julianne Dalcanton[1], Constance M. Rockosi[4], Brian Yanny[5], Heidi J. Newberg[6], Timothy C. Beers[7], Carlos Allende Prieto[8], Ron Wilhelm[9], Young Sun Lee[7], Thirupathi Sivarani[7], John E. Norris[10], Coryn A.L. Bailer-Jones[11], Paola Re Fiorentin[11], David Schlegel[12], Alan Uomoto[13], Robert H. Lupton[3], Gillian R. Knapp[3], James E. Gunn[3], Kevin R. Covey[14], J. Allyn Smith[15], Gajus Miknaitis[5], Mamoru Doi,[16], Masayuki Tanaka[17], Masataka Fukugita[18], Steve Kent[5], Douglas Finkbeiner[14], Jeffrey A. Munn[19], Jeffrey R. Pier[19], Tom Quinn[1], Suzanne Hawley[1], Scott Anderson[1], Furea Kiuchi[1], Alex Chen[1], James Bushong[1], Harkirat Sohi[1], Daryl Haggard[1], Amy Kimball[1], John Barentine[20], Howard Brewington[20], Mike Harvanek[20], Scott Kleinman[20], Jurek Krzesinski[20], Dan Long[20], Atsuko Nitta[20], Stephanie Snedden[20], Brian Lee[12], Hugh Harris[19], Jonathan Brinkmann[20], Donald P. Schneider[21], Donald G. York[22]

ABSTRACT

In addition to optical photometry of unprecedented quality, the Sloan Digital Sky Survey (SDSS) is producing a massive spectroscopic database which already contains over 280,000 stellar spectra. Using effective temperature and metallic-

[1]Department of Astronomy, University of Washington, Box 351580, Seattle, WA 98195

[2]Institute for Advanced Study, 1 Einstein Drive, Princeton, NJ 08540

[3]Princeton University Observatory, Princeton, NJ 08544

[4]University of California–Santa Cruz, 1156 High St., Santa Cruz, CA 95060

[5]Fermi National Accelerator Laboratory, P.O. Box 500, Batavia, IL 60510

[6]Department of Physics, Applied Physics, and Astronomy, Rensselaer Polytechnic Institute, 110 8th St., Troy, NY 12180

[7]Dept. of Physics & Astronomy, CSCE: Center for the Study of Cosmic Evolution, and JINA: Joint Institute for Nuclear Astrophysics, Michigan State University, East Lansing, MI 48824, USA

[8]McDonald Observatory and Department of Astronomy, University of Texas, Austin, TX 78712

[9]Department of Physics, Texas Tech University, Box 41051, Lubbock, TX 79409

[10]Research School of Astronomy & Astrophysics, The Australian National University, Cotter Road, Weston, ACT 2611, Australia

[11]Max Planck Institut für Astronomie, Königstuhl 17, 69117 Heidelberg, Germany

[12]Lawrence Berkeley National Laboratory, One Cyclotron Road, MS 50R5032, Berkeley, CA, 94720

[13]Department of Physics and Astronomy, The John Hopkins University, 3701 San Martin Drive, Baltimore, MD 21218

[14]Harvard-Smithsonian Center for Astrophysics, 60 Garden Street, Cambridge, MA 02138

[15]Dept. of Physics & Astronomy, Austin Peay State University, Clarksville, TN 37044

[16]Institute of Astronomy, University of Tokyo, 2-21-1 Osawa, Mitaka, Tokyo 181-0015, Japan

[17]Dept. of Astronomy, Graduate School of Science, University of Tokyo, Hongo 7-3-1, Bunkyo-ku, Tokyo, 113-0033, Japan

[18] Institute for Cosmic Ray Research, University of Tokyo, Kashiwa, Chiba, Japan

[19]U.S. Naval Observatory, Flagstaff Station, P.O. Box 1149, Flagstaff, AZ 86002

[20]Apache Point Observatory, 2001 Apache Point Road, P.O. Box 59, Sunspot, NM 88349-0059

[21]Department of Astronomy and Astrophysics, The Pennsylvania State University, University Park, PA 16802

[22]University of Chicago, Astronomy & Astrophysics Center, 5640 S. Ellis Ave., Chicago, IL 60637

ity derived from SDSS spectra for ∼60,000 F and G type main sequence stars ($0.2 < g - r < 0.6$), we develop polynomial models, reminiscent of traditional methods based on the UBV photometry, for estimating these parameters from the SDSS $u - g$ and $g - r$ colors. These estimators reproduce SDSS spectroscopic parameters with a root-mean-square scatter of 100 K for effective temperature, and 0.2 dex for metallicity (limited by photometric errors), which are similar to random and systematic uncertainties in spectroscopic determinations. We apply this method to a photometric catalog of coadded SDSS observations and study the photometric metallicity distribution of ∼200,000 F and G type stars observed in 300 deg^2 of high galactic latitude sky. These deeper ($g < 20.5$) and photometrically precise (∼0.01 mag) coadded data enable a measurement of the unbiased metallicity distribution for a complete volume-limited sample of stars at distances between 500 pc and 8 kpc. The metallicity distribution can be exquisitely modeled using two components with a spatially varying number ratio, that correspond to disk and halo. The best-fit number ratio of the two components is consistent with that implied by the decomposition of stellar counts profiles into exponential disk and power-law halo components by Jurić et al. (2008). The two components also possess the kinematics expected for disk and halo stars. The metallicity of the halo component can be modeled as a spatially invariant Gaussian distribution with a mean of $[Fe/H] = -1.46$ and a standard deviation of ∼0.3 dex. The disk metallicity distribution is non-Gaussian, with a remarkably small scatter (rms∼0.16 dex) and the median smoothly decreasing with distance from the plane from −0.6 at 500 pc to −0.8 beyond several kpc. Similarly, we find using proper motion measurements that a non-Gaussian rotational velocity distribution of disk stars shifts by ∼50 km/s as the distance from the plane increases from 500 pc to several kpc. Despite this similarity, the metallicity and rotational velocity distributions of disk stars are not correlated (Kendall's $\tau = -0.015 \pm 0.018$). This absence of a correlation between metallicity and kinematics for disk stars is in a conflict with the traditional decomposition in terms of thin and thick disks, which predicts a strong correlation ($\tau = -0.30 \pm 0.04$) at ∼1 kpc from the mid-plane. Instead, the variation of the metallicity and rotational velocity distributions can be modeled using non-Gaussian functions that retain their shapes and only shift as the distance from the mid-plane increases. We also study the metallicity distribution using a shallower ($g < 19.5$) but much larger sample of about two million stars in 8500 sq. deg. of sky included in SDSS Data Release 6. The large sky coverage enables the detection of coherent substructures in the kinematics–metallicity space, such as the Monoceros stream, which rotates faster than the LSR, and has a median metallicity of $[Fe/H] = -0.96$, with an

rms scatter of only ∼0.15 dex. We extrapolate our results to the performance expected from Large Synoptic Survey Telescope (LSST) and estimate that LSST will obtain metallicity measurements accurate to 0.2 dex or better, with proper motion measurements accurate to ∼0.2 mas/yr, for about 200 million F/G dwarf stars within a distance limit of ∼100 kpc ($g < 23.5$).

Subject headings: methods: data analysis — stars: statistics — Galaxy: halo, kinematics and dynamics, stellar content, structure

1. Introduction

A major objective of modern astrophysics is to understand when and how galaxies formed, and how they have evolved since then. Our own galaxy, the Milky Way, provides a unique opportunity to study a galaxy in great detail by measuring and analyzing the properties of a large number of individual stars.

The formation of galaxies like the Milky Way was long thought to be a steady process leading to a smooth distribution of stars, with this standard view exemplified by the Bahcall & Soneira (1980) and Gilmore, Wyse & Kuijken (1989) models, and described in detail by e.g. Majewski (1993). In these smooth models, the spatial distribution of stars in the Milky Way is usually[1] modeled by three discrete components described using relatively simple analytic expressions: the thin disk, the thick disk, and the halo. However, recent discoveries of complex substructure in the distribution and kinematics of the Milky Way's stars (e.g. Ivezić et al. 2000; Yanny et al. 2000; Vivas et al. 2001; Newberg et al. 2002; Gilmore, Wyse & Norris 2002; Majewski et al. 2003; Duffau, Zinn & Vivas 2006; Vivas & Zinn 2006; Grillmair 2006ab; Belokurov et al. 2006, 2007; Bell et al. 2007; Jurić et al. 2008) have deeply shaken this standard view. Unlike those smooth models that involve simple components, the new data indicate many irregular structures, such as the Sgr dwarf tidal stream in the halo and the Monoceros stream closer to the Galactic plane. These recent developments, based on accurate large-area surveys, have made it abundantly clear that the Milky Way is a complex and dynamical structure that is still being shaped by the infall (merging) of neighboring smaller galaxies.

Numerical simulations suggest that this merger process plays a crucial role in setting the structure and motions of stars within galaxies, and is a generic feature of current cosmological

[1]Infrared data towards the Galactic center require addition of a bulge and a stellar bar (e.g. Weinberg 1992; Jackson, Ivezić & Knapp 2002; and references therein).

models (e.g., Helmi et al. 1999; Springel & Hernquist 2003; Bullock & Johnston 2005). Since the individual stars that make up the stellar populations in the Milky Way can be studied in great detail, their characterization will provide clues about galaxy merging process that cannot be extracted from observations of distant galaxies (e.g., Abadi et al. 2003; Brook et al. 2004; and references therein).

The three presumably discrete Milky Way components differ not only in their spatial profiles, but also in detailed distributions of their kinematics and metallicity (e.g., Majewski 1993; Ojha et al. 1996; Freeman & Bland-Hawthorn 2002; Robin et al. 2003; Wyse 2006; and references therein). The thin disk, with a scale height of ∼300 pc, has a vertical velocity dispersion of $\sigma_z \sim 20$ km s^{-1}, while the thick disk, with a scale height of ∼1000 pc, is somewhat warmer ($\sigma_z \sim 40$ km s^{-1}) and older, has a lower average metallicity ($[Z/Z_\odot] \sim -0.7$, e.g., Gilmore & Wyse 1985), and enhanced α-element abundances (e.g., Fuhrmann 2004; Bensby et al. 2004; Feltzing 2006; Reddy et al. 2006; Ramírez et al. 2007). In contrast, the halo is composed mainly of low metallicity stars ($[Z/Z_\odot] < -1.0$, e.g., Ryan & Norris 1991), and has little or no net rotation. Hence, in addition to their spatial profiles, the main differences between these components are in their rotational velocity distributions, velocity dispersions, and metallicity distributions.

We note that a recent study by Carollo et al. (2007), based on a sample of over 20,000 stars with radial velocities from SDSS Data Release 5, has demonstrated that "the halo" of the Galaxy is likely to comprise two distinct components. According to these authors, the inner-halo component dominates the population of halo stars found at distances up to 10-15 kpc from the Galactic center (including the Solar neighborhood), and an outer-halo component dominates in the regions beyond 15-20 kpc. The inner halo stars are non-spherically distributed about the centre of the Galaxy, with an inferred axes ratio of ∼0.6, while the outer halo comprises stars that exhibit a much more spherical spatial distribution. Our present study only reaches to 8 kpc from the Sun, and hence is likely to be dominated by inner-halo stars. Therefore, for the purpose of the present paper, we assume a single component halo.

Despite the significant progress that has been made over the years, we still cannot answer some simple questions such as: Are the exponential profiles used to describe the spatial profiles of thin and thick disks an oversimplification? Why do estimates for thick disk scale height differ by a factor of several between different studies (for a discussion see Siegel et al. 2002; and Jurić et al. 2008)? Is the transition between thin and thick disks in metallicity and kinematics abrupt or continuous? Is there a large-scale metallicity gradient in the thick disk and halo? Does the disk scale length depend on metallicity? Can large spatial substructures be traced in kinematic and metallicity spaces?

To reliably answer these and similar questions, a data set needs to be both voluminous (to enable sufficient spatial, kinematic and metallicity resolution), diverse (accurate distance and metallicity estimates, as well as radial velocity and proper motion measurements are required), and faint (to probe a significant fraction of the Galaxy). Modern sky surveys, such as the Sloan Digital Sky Survey (hereafter SDSS, York et al. 2000), with its imaging and spectroscopic components, and the Two Micron All Sky Survey (Skrutskie et al. 2006) with its all-sky coverage, have recently provided such data sets.

Most studies of the Milky Way structure can be described as investigations of the stellar distribution in the nine-dimensional space spanned by the three spatial coordinates, three velocity components, and three main stellar parameters (luminosity, effective temperature, and metallicity). Depending on the quality, diversity and quantity of data, such studies typically concentrate on only a limited region of this space (e.g., the nearby solar neighborhood, pencil beam surveys, kinematically biased surveys), or consider only marginal distributions of selected quantities (e.g., number density of stars irrespective of their metallicity or kinematics, luminosity function determinations, proper motion surveys without metallicity or radial velocity information). We use the SDSS data to study in detail the stellar distribution in this multi-dimensional space. We focus on the metallicity distribution of disk and halo stars in this contribution. In companion papers we discuss the spatial distribution of stars (Jurić et al. 2008, hereafter J08) and their kinematics (Bond et al. 2008, in prep., hereafter B08).

In Section 2, we use the data for ∼60,000 probable F and G type main sequence stars provided by SDSS spectroscopic survey to calibrate a method for estimating metallicity from the $u-g$ and $g-r$ colors measured by SDSS photometric survey. Readers who are not interested in technical aspects of this method may want to skip directly to Section 3, where we apply this method to two photometric catalogs constructed using SDSS data. One catalog contains averaged repeated observations and provides improved photometric accuracy and depth to study the metallicity distribution all the way to the disk-halo interface at several kpc from the Galactic plane. The second catalog, based on all SDSS observations to date, covers a wide area and probes a significant fraction of the Galaxy. We summarize and discuss our results in Section 4.

2. Determination of Stellar Metallicity from SDSS Photometric Data

The most accurate measurements of stellar metallicity are based on spectroscopic observations. Despite the recent progress in the availability of stellar spectra (e.g., SDSS has

recently made publicly available[2] over 280,000 stellar spectra as a part of its Data Release 6, and RAVE[3] may provide up to a million spectra over the next few years), the number of stars detected in imaging surveys is vastly larger. In addition to generally providing better sky and depth coverage than spectroscopic surveys, imaging surveys obtain essentially complete flux-limited samples of stars. Such simple selection effects are advantageous when studying the Galactic structure, compared to complex targeting criteria such as for SDSS stellar spectra (see § 2.2 below). Hence, we use the SDSS spectroscopic data to calibrate a method for estimating metallicity from the SDSS imaging data, and use this calibration to study the metallicity distribution of several million Milky Way stars.

Stellar metallicity has long been estimated using photometric methods such as the traditional UV excess based δ method (Wallerstein 1962; Sandage 1969). A blue main sequence (F and G type) star's metallicity is correlated with the difference between the star's $U-B$ color and that which would be measured for a metal-rich star with the *same* $B-V$ color. This correlation is seen in both data (e.g. Carney 1979 and references therein) and detailed stellar models (Kurucz 1979). The Johnson UBV bands are similar to SDSS's ugr bands and thus it should be possible to derive an analogous method applicable to SDSS photometric system, as recently attempted by Karaali, Bilir & Tuncel (2005). However, as they pointed out, their study did not utilize SDSS data, but a somewhat different photometric system. Unfortunately, even small photometric offsets and color terms between different photometric systems may have significant systematic effects on derived metallicities. For example, the SDSS u band measurements are offset from the AB system by $\sim$0.04 mag (Eisenstein et al. 2006; Holberg & Bergeron 2006), leading to a metallicity bias of up to 0.2 dex. Here we derive photometric metallicity estimators for the SDSS filter set using SDSS Data Release 6 data. This calibration relies on the large number of stars ($\sim$287,000) with a homogeneous set of stellar parameters (effective temperature, metallicity and gravity) derived from moderate-resolution SDSS spectra (Beers et al. 2006; Allende Prieto et al. 2006; Lee et al. 2007ab; Allende Prieto et al. 2007).

2.1. An Overview of Sloan Digital Sky Survey

The SDSS is a digital photometric and spectroscopic survey which will cover about one quarter of the Celestial Sphere in the North Galactic cap, and produce a smaller area ($\sim$300 deg^2) but much deeper survey in the Southern Galactic hemisphere (Stoughton et al.

[2]See http://www.sdss.org/dr6

[3]See http://www.rave-survey.aip.de/rave

2002; Abazajian et al. 2003, 2004, 2005; Adelman-McCarthy et al. 2006). SDSS is using a dedicated 2.5m telescope (Gunn et al. 2006) to provide homogeneous and deep ($r < 22.5$) photometry in five bandpasses (Fukugita et al. 1996; Gunn et al. 1998; Smith et al. 2002; Hogg et al. 2002; Tucker et al. 2006) repeatable to 0.02 mag (root-mean-square scatter, hereafter rms, for sources not limited by photon statistics, Ivezić et al. 2003) and with a zeropoint uncertainty of ∼0.02-0.03 mag (Ivezić et al. 2004). The flux densities of detected objects are measured almost simultaneously in five bands (u, g, r, i, and z) with effective wavelengths of 3540 Å, 4760 Å, 6280 Å, 7690 Å, and 9250 Å. The large survey sky coverage will result in photometric measurements for well over 100 million stars and a similar number of galaxies[4]. The completeness of SDSS catalogs for point sources is ∼99.3% at the bright end and drops to 95% at magnitudes of 22.1, 22.4, 22.1, 21.2, and 20.3 in u, g, r, i and z, respectively. Astrometric positions are accurate to better than 0.1 arcsec per coordinate (rms) for sources with $r < 20.5$ (Pier et al. 2003), and the morphological information from the images allows reliable star-galaxy separation to $r \sim 21.5$ (Lupton et al. 2002, Scranton et al. 2002). A compendium of other technical details about SDSS can be found on the SDSS web site (http://www.sdss.org), which also provides interface for the public data access.

2.2. SDSS spectroscopic survey of stars

SDSS spectra are obtained with a pair of dual multi-object fiber-fed spectrographs on the same telescope used for the imaging survey (Uomoto et al., in prep). Spectroscopic plates have a radius of 1.49 degrees and take 640 simultaneous spectra, each with wavelength coverage 3800–9200 Å and spectral resolution of ∼2000. The signal-to-noise ratio is typically >4 per pixel at g=20.

Targets for the spectroscopic survey are chosen from the SDSS imaging data, described above, based on their colors and morphological properties[5]. The targets include

- **Galaxies:** a simple flux limit for "main" galaxies, flux-color cut for luminous red galaxies (Strauss et al. 2002, Eisenstein et al. 2001)
- **Quasars:** flux-color cut, matches to FIRST survey (Richards et al. 2002)

[4]The recent Data Release 6 lists photometric data for 287 million unique objects observed in 9583 deg^2 of sky; see http://www.sdss.org/dr6/.

[5]Recent extension of SDSS survey, known as SDSS-II, has different targeting priorities. In particular, its component known as SEGUE, is optimized for Galactic structure studies.

- **Non-tiled objects (color-selected):** calibration stars (16 per plate), "interesting" stars (hot white dwarfs, brown dwarfs, red dwarfs, red giants, blue horizontal branch stars, carbon stars, cataclysmic variables, central stars of planetary nebulae), sky

Here, *(non)-tiled objects* refers to objects that are not guaranteed a fiber assignment. As an illustration of the fiber assignments, SDSS Data Release 6 contains spectra of 791,000 galaxies, 104,000 quasars, and 287,000 stars.

The spectra are targeted and automatically processed by three pipelines:

- **target:** Target selection and tiling
- **spectro2d:** Extraction of spectra, sky subtraction, wavelength and flux calibration, combination of multiple exposures
- **spectro1d:** Object classification, redshifts determination, measurement of line strengths and line indices

For each object in the spectroscopic survey, a spectral type, redshift (or radial velocity), and redshift error is determined by matching the measured spectrum to a set of templates. The stellar templates are calibrated using the ELODIE stellar library. Random errors for the radial velocity measurements are a strong function of spectral type and signal-to-noise ratio, but are usually < 5 km s^{-1} for stars brighter than $g \sim 18$, rising sharply to $\sim$25 km s^{-1} for stars with $g = 20$. Using a sample of multiply-observed stars, Pourbaix et al. (2005) estimate that these errors may be underestimated by a factor of $\sim$1.5. Further technical details about SDSS spectroscopic survey are available from www.sdss.org.

2.3. Stellar Parameters Estimation

SDSS stellar spectra are of sufficient quality to provide robust and accurate stellar parameters such as effective temperature, gravity, and metallicity. These parameters are estimated using a variety of standard methods implemented in an automated pipeline (SEGUE Stellar Parameters Pipeline; Beers et al. 2006). A detailed discussion of these methods and their performance can be found in Allende Prieto et al. (2006, 2007) and Lee et al. (2007ab). Based on a comparison with high-resolution abundance determinations, they demonstrate that the combination of spectroscopy and photometry from SDSS is capable of delivering estimates of $T_{\rm eff}$, $log(g)$, and $[Fe/H]$ with *external accuracies* of 190 K (3.2 %), 0.28 dex, and 0.17 dex, respectively. These tests indicate that *mean systematic errors* for $[Fe/H]$ and $T_{\rm eff}$

should not be larger than about 0.2 dex and 100 K, and may be below 0.1 dex and 75 K (Lee et al. 2007b). Note that these estimates apply to stars with a wider range of temperatures than we consider in this study.

We use the final adopted values, called $teffa$ and $feha$ in the SDSS *sppParams* table, that are based on averaging several different methods. A detailed analysis by Lee et al. (2007ab) demonstrates that systematic metallicity differences between the methods used in averaging do not exceed ∼0.1 dex. A comparison with Galactic open and globular clusters indicates that the adopted metallicity scale systematically overestimates metallicity by ∼0.15 dex for $[Fe/H] < -2$ and underestimates metallicity by up to ∼0.3 dex for stars near solar metallicity.

Only a few percent of stars in SDSS spectroscopic sample are giants. For this reason we study only the main sequence stars, using selection criteria described below. Although we address photometric estimates of effective temperature, the main goal of this section is to derive a robust and accurate photometric metallicity estimator.

2.3.1. Sample Selection

We begin by selecting bright stars from the main stellar locus (Lenz et al. 1998; Fan 1999;, Finlator et al. 2000; Smolčić et al. 2004), with colors located in the proper range for the application of photometric metallicity method (roughly[6] $0.4 < B - V < 0.8$, Carney 1979), and from sky regions with modest interstellar dust extinction (SDSS utilizes the Schlegel, Finkbeiner & Davis 1998 maps). The specific criteria applied to 130,620 entries from the so-called *sppParams* table[7] that have $log(g) > 0$ are

1. the interstellar extinction in the r band below 0.3: [106,816]
2. $14 < g < 19.5$: [104,844]
3. $0.2 < (g - r) < 0.6$: [75,928]
4. $0.7 < (u - g) < 2.0$ and $-0.25 < (g - r) - 0.5(u - g) < 0.05$: [68,306]
5. $-0.2 < 0.35(g - r) - (r - i) < 0.10$: [66,496]

[6]At the ∼0.05 mag accuracy level, $B - V$=0.949$(g - r)$+0.20, for more accurate (<0.01 mag) transformations see Ivezić et al. (2006a).

[7]Available from http://www.sdss.org/dr6/products/spectra/spectroparameters.html

The number in brackets indicates the number of stars left after each selection step.

Using the photometric parallax relation from J08 (their "bright" normalization),

$$M_r = 3.2 + 13.30\,(r-i) - 11.50\,(r-i)^2 \\ +5.40\,(r-i)^3 - 0.70\,(r-i)^4, \quad (1)$$

we further limit the sample to 64,275 stars in the 1–10 kpc range. Due to the small $r-i$ color range spanned by F/G stars, when computing M_r we interpolate the $r-i$ colors from the better measured $g-i$ colors using a stellar locus relation[8]

$$g-r = 1.39(1-\exp[-4.9(r-i)^3 \\ -2.45(r-i)^2 - 1.68(r-i) - 0.050]). \quad (2)$$

The selected stars span the 5000–7000 K temperature range (with a median of 5,900 K) and 99.4% have metallicity in the range −3 to 0 (with a median of −1.0). While the sample is dominated by main sequence stars (the median log(g) is 4.1, with an rms scatter of 0.44 dex), a small fraction of stars have gravity estimates consistent with giants (see Figure 1). We exclude 4% of stars with log(g)<3 (which typically have lower metallicity than dwarfs, with a median of −1.5, c.f. Figure 1), but without a significant effect on results. This fraction of giants is relatively high because the $g-r \sim 0.5$ color range, where the fraction of giants is the highest, was deliberately targeted for SDSS spectroscopy; about 7% of stars in the sample with $0.4 < g-r < 0.6$ have log(g)<3.

2.3.2. Effective Temperature

The dependence of the median effective temperature and metallicity on the position in the $g-r$ vs. $u-g$ color-color diagram for the final sample of 61,793 stars is shown in Figure 2. The top left panel demonstrates that the effective temperature, $T_{\rm eff}$, can be determined from the $g-r$ color alone, with a negligible dependence on the $u-g$ color (the gradient of $\log(T_{\rm eff})$ with respect to the $g-r$ color is at least ~ 60 times as large as the gradient with respect to the $u-g$ color). This difference in gradients is due to a general insensitivity to metallicity

[8]J08 use a maximum likelihood projection on the mean stellar locus, which avoids this problem. At the bright end relevant here, the two methods produce essentially the same results and we opted for the simpler one. It turns out that the J08 $M_r = f(r-i)$ relation (eq. 1) and the stellar locus relation (eq. 2) can be combined into a single relation, $M_r = 2.62 + 4.63\,(g-i) - 1.68\,(g-i)^2 + 0.395\,(g-i)^3$, that agrees with eqs. 1 and 2 with an rms scatter of 0.05 mag for $0.2 < g-i < 3.4$.

of relationships between effective temperature and colors at wavelengths longer than 0.4 μm (Sandage & Smith 1963; Mannery & Wallerstein 1971). The best-fit expression

$$\log(T_{\rm eff}/{\rm K}) = 3.872 - 0.264\,(g-r) \tag{3}$$

reproduces SDSS spectroscopic temperature for 61,793 main sequence stars selected from the $0.2 < g-r < 0.6$ color range with an rms scatter of 0.007 dex (corresponding to ∼100 K). When residuals are binned in 0.01 mag wide $g-r$ bins, the largest median residual is 0.003 dex (∼40 K at the median temperature of 5900 K), demonstrating that a linear fit is sufficient. When residuals are binned in 0.1 dex wide metallicity bins, the largest median residual is also 0.003 dex. There is no discernible dependence of residuals on metallicity for stars with $[Fe/H] < -1$, while for stars with $-1 < [Fe/H] < -0.5$ a gradient of $log(T)$ is 0.008 per decade of metallicity (dex/dex) is present.

This behavior is consistent with results based on temperatures derived with the infrared flux method (Ramírez & Meléndez 2005; Casagrande, Portinari & Flynn 2006, hereafter CPF). For example, the expression for effective temperature as a function of $B-V$ color and metallicity from CPF predicts an effective temperature of 5700 K for $B-V = 0.6$ ($g-r$=0.425) and metallicity of −1.0, with the latter corresponding to the median metallicity of stars in the SDSS spectroscopic sample. The effective temperature predicted by eq. 3 is 5750 K (a discrepancy of 0.004 dex), and the median spectroscopic temperature for stars with $0.42 < g-r < 0.43$ is 5730 K. We note that both the CPF relation and Ramírez & Meléndez (see Figs. 1 and 10) predict a steeper dependence of effective temperature on metallicity: at $B-V = 0.6$ the predicted effective temperature increases by 180 K as metallicity increases from −1.5 to −0.5, while in SDSS spectroscopic sample the corresponding temperature increase is 50 K. Discrepancies with the expression proposed by Sekiguchi & Fukugita (2000) are somewhat larger. Their effective temperature scale is colder by ∼130 K than the SDSS scale, and $\log(T_{\rm eff})$ residuals are correlated with metallicity and log(g) with gradients of about 0.01 dex/dex. Further details about the behavior of photometric temperature estimator are discussed in Appendix A.

2.3.3. Metallicity

As first suggested by Schwarzschild, Searle & Howard (1955), the depletion of metals in a stellar atmosphere has a detectable effect on the emergent flux, in particular in the blue region where the density of metallicity absorption lines is highest (Beers & Christlieb 2005, and references therein). The median metallicity of stars selected from the SDSS spectroscopic sample as a function of the $u-g$ and $g-r$ colors shows a complex behavior that is consistent

with expectations: the detailed dependence of the UV excess (i.e. the $u-g$ color) on metallicity varies with effective temperature (i.e. the $g-r$ color). Even when the $g-r$ vs. $u-g$ plane is separated by $g-r=0.4$ into two regions suggested by the metallicity map, at least second order polynomials or several piecewise linear fits are required to avoid systematic errors larger than 0.1 dex. In order to do so for the entire map with a single function, we find that third-order terms are required and model the map as

$$[Fe/H]_{ph} = A + Bx + Cy + Dxy + Ex^2 + Fy^2 + Gx^2y + Hxy^2 + Ix^3 + Jy^3, \qquad (4)$$

where

- $x=(u-g)$ for $(g-r)\leq 0.4$, and $x=(u-g)-2(g-r)+0.8$ for $(g-r)>0.4$ (this dual definition is required to describe the map with a single set of coefficients A–J)
- $y=(g-r)$, and
- (A–J) = (−4.37, −8.56, 15.5, −39.0, 23.5, 20.5, 12.1, 7.33, −10.1, −21.4).

This expression describes the median metallicity map shown in the top right panel in Figure 2 with a root-mean-square (rms) scatter of 0.09 dex. This level of systematic calibration errors is negligible compared to random errors per star ($\sim$ 0.2 dex, due to photometric errors) discussed below, and is comparable to systematic errors in SDSS spectroscopic metallicity estimates. A map of the median residuals, when fitting the median metallicity map using eq. 4, in the $g-r$ vs. $u-g$ plane is shown in the bottom left panel in Figure 2. It illustrates that there is no strong correlation between systematic errors in photometric metallicity computed with eq. 4 ($\lesssim$0.1 dex) and the $u-g$ and $g-r$ colors.

We compute photometric metallicity for all 61,793 stars in the sample using eq. 4 and compare it to spectroscopic metallicity. The rms scatter of metallicity residuals is 0.24 dex (determined from interquartile range), and the distribution of residuals is only slightly non-Gaussian (97% of the sample is contained within $\pm 3\sigma$ range).

The rms scatter of metallicity residuals depends on both brightness and color. The bottom right panel in Figure 2 illustrates the color dependence: for low-metallicity stars the rms increases to $\lesssim$0.3 dex, while it is about 0.15 dex or less for high-metallicity stars. This is expected due to weaker spectral lines in low-metallicity stars (e.g., Du et al. 2004; Keller et al. 2007).

The rms scatter of metallicity residuals increases with the g band magnitude from 0.18 dex for g <17, to 0.25 dex at $g=18$, and 0.45 dex at $g=19.5$. The random metallicity errors are dominated by the errors in the u band magnitudes. The ratio of this scatter to

the scatter expected due to photometric errors (which is readily computed from eq. 4) is 1.7, and is nearly independent of magnitude. The implied *random* errors in spectroscopic and photometric metallicity are thus comparable and have similar signal-to-noise properties. In particular, we estimate that random errors in spectroscopic metallicity increase from 0.15 dex for $g < 17$ to 0.36 dex at $g = 19.5$ (for comparison, the corresponding values for photometric metallicity are 0.10 dex and 0.30 dex). The seemingly surprising result that the estimated errors for photometric metallicity are *smaller* than for spectroscopic metallicity, despite the former being calibrated off the latter, is due to averaging of *many* spectroscopic estimates in a given small color-color bin when calibrating photometric metallicity, and the fact that the signal for photometric metallicity predominantly comes from wavelengths shorter than 0.4 μm, while for spectroscopic metallicity from longer wavelengths.

This error behavior limits the application of photometric metallicity estimates based on SDSS data to about $g < 19.5$. This limit is essentially set by the precision of the u band photometry ($u < 20.5$). Somewhat coincidentally[9], this is about the same limiting depth as for SDSS spectroscopic sample (the spectroscopic targeting limit for the SEGUE survey is $g < 20$). Despite this limitation, the photometric metallicity estimator given by eq. 4 is a valuable tool because it allows metallicity to be determined for *all* main sequence SDSS stars in the $0.2 < g - r < 0.6$ color range. For example, in SDSS DR6, out of ∼5.7 million point sources from this color range that are brighter than $g = 19.5$, SDSS spectra classified as stars are available only for ∼94,000. This implies a sample size increase by a factor of 60 when using photometric metallicity. Furthermore, when deeper data are available, the photometric metallicity estimator can be used to study metallicity distribution to distances beyond the reach of main sequence stars in spectroscopic sample (a small number of giants in spectroscopic sample, that reach ∼100 kpc, cannot be easily recognized using photometry alone; however, see Helmi et al. 2003). Further details about the behavior of photometric metallicity estimator are discussed in Appendix B.

3. Analysis of Stellar Photometric Metallicity

We now utilize the photometric metallicity estimator developed above to study the stellar metallicity distribution as a function of position in the Galaxy and stellar kinematics. We consider stars in a restricted color range, $0.2 < g - r < 0.4$, because the redder stars ($0.4 < g - r < 0.6$) do not extend as far into the halo (due to smaller luminosity, see Table

[9]The similar depths are not entirely independent as they both reflect the atmospheric and sky properties, and various scientific tradeoffs, but this discussion is beyond the scope of this paper.

1). The small color range also minimizes various selection effects that could be larger for a wider color/luminosity range (such as uncertainties in photometric parallax relation and contamination by giants). As an additional motivation, in this color range metallicity is nearly a function of the $u-g$ color alone (eq. 2 in Appendix B), which allows a simple assessment of the impact of photometric errors in the u band on derived metallicity.

The adopted $0.2 < g-r < 0.4$ color range spans about 10 MK spectral subtypes (from ∼F5 to ∼G5, Bailer-Jones et al. 1997, 1998). The absolute magnitudes can be estimated using a photometric parallax relation from J08 (we adopt their "bright" normalization). The median absolute magnitude in this color range is $M_g = 4.4$, with an rms scatter of 0.3 mag and a difference of ∼1.2 mag in M_g between the blue and red ends. The adopted photometric parallax relation does not take into account the dependence of absolute magnitude on metallicity, which we address below in § 3.4.5.

We consider two photometric catalogs constructed using SDSS data. A catalog of coadded repeated observations (10 on average, Ivezić et al. 2007), known as the SDSS Stripe 82 catalog, provides improved photometric accuracy to a fainter flux limit in ∼300 deg^2 of sky. For example, while single-epoch SDSS data deliver a median $u-g$ error of 0.06 mag at $g = 19.5$ (for point sources with $0.2 < g-r < 0.4$), the same level of accuracy is extended to beyond $g = 20.5$ in the coadded catalog. This allows us to study metallicity distribution all the way to the disk-halo interface at several kpc from the Galactic plane with small metallicity errors. At the bright end, the random errors in the $u-g$ error are 0.01 mag in the coadded catalog and 0.025 mag in single-epoch data (an error in the $u-g$ color of 0.02 mag induces a metallicity error in $[Fe/H]$ that varies from 0.02 dex at $[Fe/H] = -0.5$ to 0.11 dex at $[Fe/H] = -1.5$). This improvement in photometric metallicity accuracy by more than a factor of 2 enables robust estimates of the metallicity distribution width for disk stars. However, an important disadvantage of using the coadded catalog is its very small sky coverage. Hence, we extend our study to a significant fraction of the Galaxy by utilizing a wide-area catalog based on SDSS Data Release 6 (DR6 catalog, hereafter). This catalog covers a ∼30 times larger area than the deep coadded catalog, at the expense of a ∼1 mag shallower sample.

We begin our analysis with a discussion of the stellar distribution in the g vs. $u-g$ color-magnitude diagram, which reveals several features that are central to the conclusions of this paper. While this diagram maps well to a distance vs. metallicity plane, as discussed in § 3.2 further below, we chose to first describe these features using directly observed quantities. When discussing positions of stars in the Milky Way, we use the usual cylindrical coordinate system (R, ϕ, Z) aligned with the Galactic center (assumed to be at a distance of 8.0 kpc) and the Z axis towards the north Galactic pole. For projections parallel to the Galactic

plane, we follow J08 and use right-handed X and Y coordinates, with the Sun at $X = 8.0$ kpc and the positive Y axis pointing towards $l = 270$.

3.1. The Bimodal $u - g$ Distribution of F/G Stars

We selected 110,363 sources from ∼1.01 million entries in the Stripe 82 coadded catalog[10] by requiring at least 4 detections in the u band, $0.20 < g - r < 0.40$ and $g < 20.5$. These sources have $|\delta_{J2000}| < 1.266°$ and right ascension in the range 20h 34m to 4h 00m. For reference, Galactic coordinates, (l,b), are (46,−24), (96,−60) and (190,−37) for α_{J2000}=−50°, 0° and 60° (at δ_{J2000}=0°).

The distribution of these stars in the g vs. $u - g$ color-magnitude diagram is shown in the top left panel in Figure 3. A bright red ($g < 18$, $u - g \sim 1.1$) and a faint blue ($g > 18$, $u - g \sim 0.9$) feature are clearly discernible, and are roughly separated by the $u - g = 1$ line (corresponding to $[Fe/H] \sim -1.0$). The marginal $u - g$ distributions for three g slices are shown in the bottom left panel. They can be approximately described by a sum of two ∼0.07 mag wide Gaussians centered on $u - g$=0.90 and 1.07, with the number ratio of the blue to red component increasing with magnitude from 1:7 in the bright bin to 20:1 in the red bin. The blue and red components correspond to distant metal-poor halo stars, and more metal-rich and closer disk stars, respectively, as discussed further below. The width of 0.07 mag is sufficiently larger than the median error in the $u - g$ color (0.05 mag at g=20.5, 0.04 at g=20, 0.02 at g=19 and 0.01 at g=17.5) to provide a robust measure of the intrinsic width of the $u - g$ distribution.

In addition to an overall blueing of the median $u-g$ color towards the faint end induced by the varying number ratio of the two components, *the median u−g color for each component also becomes bluer*, as illustrated in Figure 4 and summarized in Table 2. We measure gradients of −0.012 mag/mag for the disk component[11] ($14.5 < g < 17$) and −0.006 mag/mag for the halo component ($18 < g < 20.5$), with statistical errors of ∼0.002 mag/mag. Using an approximate mapping from magnitude to distance, these color differences could be produced by a gradient of roughly 0.02 mag/kpc between $Z = 1$ kpc and 2.5 kpc for disk stars, and 0.003 mag/kpc between $Z = 4$ kpc and 10 kpc for halo stars. Hence, the color gradient *per kpc* is about 7 times larger for disk stars.

[10]This catalog is publicly available from http://www.sdss.org/dr6/products/value_added/index.html.

[11]This gradient was accounted for in the definition of the s color by Ivezić et al. (2004), but its meaning was not understood at that time.

The detected color gradient cannot be caused by potential errors in the applied corrections for interstellar extinction (Schlegel, Finkbeiner & Davis, 1998). The median value of the $u-g$ reddening correction is only 0.05 mag, and even the closest stars (at 500 pc) are well beyond the ∼100 pc thick dust layer (J08). Such a gradient (∼0.05 mag between $u=14$ and $u=19$) could be caused by a non-linearity in the u band measurements (based on a comparison with independently measured Stetson's standard stars, this effect is ruled out for the g band measurements, Ivezić et al. 2007). However, a u band non-linearity at the 0.05 mag level is excluded by *in situ* measurements of the hardware response curve, and a comparison of reductions of SDSS data using several different pipelines (SExtractor, DAOPhot and DoPhot; Becker et al. 2007) excludes such a large software error in SDSS photometric pipeline. We proceed with an assumption that this gradient is not a problem in SDSS data.

For selected stars with $0.2 < g-r < 0.4$, the $u-g$ color measures metallicity (see Appendix B) and the observed color scatter and color gradients correspond to metallicity distribution width and metallicity gradients. Because the imaging sample is defined by a simple flux limit, these measurements are relatively easy to interpret. On the contrary, the SDSS spectroscopic sample has an extremely biased distribution in the g vs. $u-g$ color-magnitude diagram, as illustrated in two right panels in Figure 3, and it would not be easy to derive a robust selection function. Using eqs. 1 and 4, we find that the color gradients measured for the imaging sample roughly correspond to a ∼0.06 dex/kpc metallicity gradient for disk stars at Z∼1.5 kpc, and a ∼0.01 dex/kpc for halo stars in the Z=4-10 kpc range (given the distance and sky coordinates, the three-dimensional position in the Galaxy can be trivially computed). In the remainder of this section we remap the g vs. $u-g$ color-magnitude diagram to a distance-metallicity diagram, and discuss the metallicity distribution as a function of the position in the Galaxy, develop a model that captures the data behavior, and correlate metallicity with kinematics.

3.2. The Bimodal Metallicity Distribution of Thick Disk and Halo Stars

Despite its small area, the Stripe 82 catalog covers a substantial range of R and Z, as shown in the top left panel in Figure 5. As evident from the dependence of the median metallicity on R and Z, the Z gradient is much larger than the radial gradient (by about a factor of 10). Given this large difference in metallicity gradients, we proceed by making the assumption that the metallicity distribution is a function of the Z coordinate only (in § 3.5 below, we critically examine and justify this assumption using the DR6 catalog). To further minimize the effect of any radial gradient, we constrain the sample to ∼30,000 stars with

$7 < R/\mathrm{kpc} < 9$.

The top right panel in Figure 5 shows the resulting conditional metallicity probability distribution for a given Z, $p([Fe/H]|Z)$. This distribution is computed as metallicity histograms in narrow Z slices, and normalized by the total number of stars in a given slice. Apart from renormalization and the applied $7 < R/\mathrm{kpc} < 9$ selection, this is essentially an upside-down warped version of the g vs. $u-g$ color-magnitude diagram shown in the top left panel in Figure 3. The bright red and faint blue components from Figure 3 are now readily identifiable as relatively close metal-rich disk component and more distant metal-poor halo component.

3.3. A Simple Model for the Conditional Metallicity Probability Distribution

As evident from the $p([Fe/H]|Z)$ map shown in top right panel in Figure 5, the Z gradient of the median metallicity map shown in the top left panel in Figure 5 is due to varying contributions of a metal-rich disk component and a metal-poor halo component. We first attempt to model the $p([Fe/H]|Z)$ map using two Gaussian components with a Z-dependent ratio of their area (components' number ratio)

$$p(x = [Fe/H]|Z) = (1 - f_H)G(x|\mu_D, \sigma_D) + f_H G(x|\mu_H, \sigma_H), \quad (5)$$

where

$$G(x|\mu, \sigma) = \frac{1}{\sqrt{2\pi}\sigma} \mathrm{e}^{\frac{-(x-\mu)^2}{2\sigma^2}}. \quad (6)$$

The distribution width for both components can be modeled as spatially invariant, $\sigma_D = 0.16$ dex, and $\sigma_H = 0.30$ dex, as is the case for the median halo metallicity, $\mu_H = -1.46$. The median and dispersion for metallicity distribution of halo stars is in good agreement with previous work (e.g., Ryan & Norris 1991). Due to small errors in the $u-g$ color for coadded data, the contribution of measurement errors to σ_D and σ_H is very small: the implied intrinsic widths are 0.16 dex and 0.29 dex, respectively.

Inspection of the $p([Fe/H]|Z)$ map suggests that the variation of the median metallicity for the disk component[12] in the $0.5 < |Z|/\mathrm{kpc} < 5$ range can be described as

$$\mu_D(Z) = \mu_\infty + \Delta_\mu \exp(-|Z|/H_\mu) \text{ dex}, \quad (7)$$

[12]An obvious question is whether the observed variation of the median metallicity for the disk component simply reflects the varying contributions of thin and thick disk stars. This question in addressed in detail in § 3.4.4.

with the best-fit values $H_\mu = 1.0$ kpc, $\mu_\infty = -0.78$ and $\Delta_\mu = 0.35$. The best fit is shown by the curved dashed line in the top right panel in Figure 5. The exponential "height", H_μ, is constrained to only about 50% due to covariances with μ_∞ and Δ_μ (which are constrained to about 0.05 dex). The implied median metallicity values agree well with a value of -0.7 obtained by Gilmore & Wyse (1985), while they did not detect a metallicity gradient.

The best-fit $\mu_D(Z)$ given by eq. 7 is valid only for $|Z| > 500$ pc because of the sample bright flux limit. Close to the plane, the mean and rms scatter of metallicity distribution are -0.14 and 0.19 for F/G type dwarfs (Nordström et al. 2004; Allende Prieto et al. 2004), and -0.12 and 0.18 for K type giants (Girardi & Salaris 2001). Hence, the vertical metallicity gradient close to the plane must be larger than ~ 0.35 dex/kpc implied by the *extrapolation* of eq. 7 (because stars on average become more metal poor by about 0.5 dex between $Z = 0$ and $|Z| = 1$ kpc).

To set the relative normalization of the two Gaussians, $f_H(Z)$, we approximately separate disk and halo components by isolating stars above and below $[Fe/H] = -1$. A good description of the data, shown by symbols in Figure 6, is provided by a best-fit function with three free parameters

$$f_H(Z) = \frac{1}{1 + a \exp[-(|Z|/b)^c]}, \tag{8}$$

with $a = 70$, $b = 300$ pc, and $c = 0.63$. We discuss this function further in § 3.3.4.

3.3.1. The "metal-weak thick disk": a third Gaussian component or a non-Gaussian Distribution?

The difference between the data and a two-Gaussian model described above is shown in the bottom left panel in Figure 5. As evident, the overall behavior of the two dominant components is captured, but the residual map reveals a feature that contains intermediate-metallicity stars ($[Fe/H] \sim -1.0$) within ∼2-3 kpc from the plane. This feature includes about 5% of stars in the sample and is reminiscent of the so-called "metal-weak thick disk" (Morrison, Flynn & Freeman 1990; Chiba & Beers 2000; Beers et al. 2002). Indeed, it can be satisfactory modeled as a third Gaussian component with $\mu = -1.0$, $\sigma = 0.10$ dex and a strength of 20% relative to the metal-rich component, as illustrated by the smooth residual map shown in the bottom right panel in Figure 5.

An alternative to postulating a third Gaussian component for eq. 5 is to adopt a skewed metallicity distribution for the disk component whose shape need not vary with the distance from the plane (i.e. replacing $G(x|\mu_D, \sigma_D)$ with a non-Gaussian distribution). A skewed shape for the metallicity distribution of local F/G dwarfs was also measured by Gilmore,

Wyse & Jones (1995), but with an overall offset of ∼0.5 dex towards higher metallicity, as would be expected compared to our data at $|Z| = 1$ kpc.

A quantitative validation of such a universal shape for the disk metallicity distribution is shown in Figure 7. In each Z slice that shows evidence for disk component, the shape of its skewed metallicity distribution can be modeled[13] as a sum of two Gaussians with fixed positions relative to each other (offset of 0.1 dex), fixed widths (0.21 dex for the more metal poor component, and 0.11 dex for the other), and fixed relative normalization (1.7-to-1 number ratio in favor of the more metal poor component). The values of these four parameters were obtained by *simultaneously* fitting the four histograms shown in Figure 7, with the position of the disk distribution fixed at values computed from eq. 7 (the difference between the median given by eq. 7 and the mean for the more metal poor disk Gaussian is 0.067 dex). The halo parameter f_H was initially estimated using eq. 8, while $\mu_H = -1.46$ and $\sigma_H = 0.30$ were kept constant. A few minor adjustments to these parameters for bins with $|Z| < 4$ kpc, listed in Table 3, improved the fits. The most notable change is a shift of the halo metallicity distribution by 0.08 dex towards lower values.

The best-fit values of f_H from Table 3 are consistent with eq. 8. By retaining that function, and adopting the above Z-independent two-Gaussian shape description for the disk component, we obtain residual map that is indistinguishable from that obtained using a third Gaussian component. Hence, we conclude that either hypothesis can explain the data. While both are formally based on three Gaussian components, the "universal shape" hypothesis demonstrates that the data do not require the second disk Gaussian to be independent of the first.

It is tempting to identify the two Gaussians that describe the disk component with the thin and thick disk contributions. However, the fits presented above are inconsistent with this interpretation. The double-exponential best-fit to observed spatial profile (with scale heights of 245 pc and 743 pc, and a relative normalization of 0.13, see § 3.3.4 and Figure 6) imply that the ratio of thick-to-thin disk stars should strongly vary from 0.5 in the $Z = 0.5-1.0$ kpc bin to > 100 in the $Z = 3.0-4.0$ kpc bin. Yet, the metallicity distributions admit a fit based on a *constant normalization ratio* for the two Gaussian components. Of course, this fitting success alone does not necessarily prove that traditional decomposition into two fixed distributions with a varying normalization ratio is inconsistent with the data. We return to the problem of distinguishing these two hypothesis, that have very different implications for galaxy formation and evolution theories, when discussing correlations with

[13]We attempted to fit this skewed distribution using a log-normal distribution but the detailed shape could not be reproduced.

kinematics further below (§ 3.4.4).

3.3.2. Effects of Systematic Errors in the Photometric Parallax Relation

Various systematic errors in metallicity and distance estimates affect the best-fit models for the metallicity distribution described above. The main sources of systematic errors in adopted photometric parallax relation are metallicity and binarity effects (the age effects can contribute at most 0.3 mag systematic uncertainty in absolute magnitude at the median color of the sample, $g - r = 0.3$, and ∼0.1 mag at $g - r = 0.4$). For example, the Laird, Carney & Latham (1988, LCL hereafter) metallicity correction implies an absolute magnitude brightening of about 1 mag/dex for F/G stars. The adopted photometric parallax relation is calibrated to low-metallicity stars at its blue end (J08). We have investigated the impact of metallicity on the results from previous section by adding to the right side of eq. 1 a correction

$$\Delta M_r = -0.75\,([Fe/H] + 1.5). \tag{9}$$

This relation is similar to the prescription[14] given by LCL, and agrees well with a kinematic analysis described below. Its effect is to increase estimated distance to disk stars by about 30% on average, and to correct for systematic errors in distances to halo stars.

The net impact of metallicity correction is detectable but minor, and analogous to an increase of the disk exponential scale height by ∼30%. The largest change of $f_H(Z)$ (eq. 8) is below 0.05, and it is confined to the $1 < |Z|/\mathrm{kpc} < 2$ range. The change of median metallicity is below 0.05 dex for both components.

As discussed in detail by J08, the binarity effects are expected to decrease the inferred distances and disk exponential scale height by about 15%, so the metallicity and binarity effects partially cancel each other. The impact of binarity on metallicity determination is hard to estimate without detailed knowledge of the incidence frequency and the mass ratio distribution of binaries. By performing simulations similar to those described by J08, we find that the worst case scenario is a system consisting of a luminous low-metallicity primary with $u - g = 0.8$ and $g - r = 0.2$, and a secondary with $u - g \sim 1.0$ and $g - r = 0.5$ (the redder secondaries are too faint to have a larger impact). When such a system is (mis)interpreted as a single star, the distance is underestimated by 15%, the effective temperature is underestimated by ∼240 K, and the metallicity is overestimated by ∼0.2

[14]The LCL metallicity correction depends on color. However, for the restricted range of colors discussed here, the effect of color on M_r is about 10 times smaller than the effect of metallicity.

dex. For components that have the mass ratio closer to unity (as suggested by, e.g., Reid et al. 2002), the bias in metallicity will be much smaller, while the bias in distance estimate can increase up to ∼40%.

3.3.3. The Edge of Thick Disk at $|Z| \sim 5$ kpc?

Using photographic data for 250 stars, Majewski (1992) advocated an "edge" of the Galactic thick disk at about 5.5 kpc above the Galactic plane. Indeed, the map of conditional metallicity distribution shown in the top right panel in Figure 5 suggests a tantalizing possibility that the metal-rich component does not extend beyond 4–5 kpc from the plane. This visual impression is addressed quantitatively by the histogram shown in the bottom right panel in Figure 7. The extrapolation of disk component to the 5–7 kpc bin predicts that disk should be detectable as a factor of ∼2 excess around $[Fe/H] \sim -0.8$, on top of the underlying halo distribution. Such an excess seems consistent with the data and argues against a cutoff in the distribution of disk stars. Due to a small sample size (∼4,800 stars), the noise is large and the significance of this excess is not overwhelming. Even when the $7 < R/\mathrm{kpc} < 9$ constraint is removed, the $5 < |Z|/\mathrm{kpc} < 7$ subsample is still too small (∼8,600 stars) to significantly overcome counting noise.

We conclude that Stripe 82 catalog is not sufficiently large to convincingly demonstrate the lack of an edge in the distribution of disk stars. We improve the statistical power of this analysis by using a ∼30 times larger sky coverage provided by DR6 catalog, as discussed below.

3.3.4. A comparison with results from Jurić et al. (2008)

The expression given by eq. 8 is only a convenient fit that involves a small number of free parameters. The halo-to-disk number ratio, f_H, depends on disk and halo spatial profiles, both of which are usually modeled using numerous free parameters. As discussed by J08, a unique solution is not possible without a large sky coverage, and even in such a case it is difficult to obtain it. Nevertheless, we can test whether the data for f_H discussed here are *consistent* with the best-fit spatial profiles obtained by J08, *that do not incorporate metallicity information*.

J08 show that the stellar number density distribution, $\rho(R, Z, \phi)$ can be well described (apart from local overdensities) as a sum of two cylindrically symmetric components

$$\rho(R, Z, \phi) = \rho_D(R, Z) + \rho_H(R, Z). \quad (10)$$

The disk component can be modeled as a sum of two exponential disks

$$\rho_D(R,Z) = \rho_D(R_\odot,0)\left[\mathrm{e}^{-|Z+Z_\odot|/H_1-(R-R_\odot)/L_1} + \epsilon_D \mathrm{e}^{-|Z+Z_\odot|/H_2-(R-R_\odot)/L_2}\right], \quad (11)$$

and the halo component requires an oblate power-law model

$$\rho_H(R,Z) = \rho_D(R_\odot,0)\,\epsilon_H \left(\frac{R_\odot^2}{R^2+(Z/q_H)^2}\right)^{n_H/2}. \quad (12)$$

The best-fit parameters are discussed in detail by J08. We have adopted the following values for parameters relevant in this work (second column in Table 10 from J08): $Z_\odot$=25 pc, $H_1 = 245$ pc, $H_2 = 743$ pc, $\epsilon_D = 0.13$, $\epsilon_H = 0.0051$, $q_H = 0.64$, and $n_H = 2.77$.

The fraction of halo stars implied by this model,

$$f_H(R,Z) = \frac{\rho_H(R,Z)}{\rho_D(R,Z)+\rho_H(R,Z)}, \quad (13)$$

agrees reasonably well with f_H determined here (see Figure 6) *without any modification*. Given that J08 determined their best-fit parameters using counts at $Z \gtrsim 10$ kpc, this agreement is remarkable. The short-dashed line representing the J08 model in Figure 6 can be brought in essentially perfect agreement with data points by increasing H_2 and ϵ_H by 15% of their values (i.e. by less than their uncertainty, 20%, quoted by J08). This modified model is shown by the dot-dashed line in Figure 6. Alternatively, data points can be moved closer to the J08 model by adjusting the disk–halo metallicity separation boundary, at $[Fe/H] = -1$, by 0.05-0.1 dex.

The best-fit model for stellar counts provides a useful guidance that the counts of thin and thick disk stars become equal around $|Z| \sim 1$ kpc, and that the counts of disk and halo stars become equal around $|Z| \sim 3$ kpc. At the bright end of the sample at 500 pc, thin disk stars contribute ∼70% of stars to the disk component (with a halo contribution of ∼2%), and at the faint end at 5 kpc, halo stars contribute ∼90% of the sample. Hence, the SDSS imaging data are well suited for studying metallicity distribution all the way from thin disk to halo, through thick disk transition, using an essentially complete flux-limited sample of numerous main sequence stars.

3.4. Analysis of the Wide SDSS DR6 Sample

SDSS Data Release 6 provides photometry for ∼300 million objects detected in ∼10,000 sq.deg. of sky. Using selection criteria listed in § 2.3.1, and $g < 19.5$, we selected 2.48 million stars (the extended $0.2 < g-r < 0.6$ color range includes 5.7 million stars). The significantly

increased sky coverage comes at the expense of photometric metallicity precision: for metal-rich disk stars random errors increase from 0.05 dex at a distance of 1 kpc to 0.12 dex at 4 kpc, and for metal-poor halo stars they increase from 0.20 dex at 4 kpc to 0.36 dex at 7 kpc (about 3 times as large as for coadded data discussed above).

The median metallicity map shown in the top left panel in Figure 8 is analogous to that shown in Figure 5 except for the significantly larger sky coverage. The conclusion about the vertical metallicity gradient being much stronger than the radial gradient remains valid. The strong Z gradient is a result of the low-metallicity halo component becoming dominant at Z beyond $\sim$3 kpc.

The conditional metallicity distribution for DR6 stars from a solar cylinder with a radius of 1 kpc is shown in the bottom right panel in Figure 8. As evident, there is a close resemblance between the conditional metallicity distribution map constructed using the Stripe 82 catalog (Figure 5) and the map based on the DR6 catalog. The best-fit parameters listed in Table 3 that describe histograms shown in Figure 7 are consistent with the DR6 map, when the increased measurement errors are taken into account (disk and halo components convolved with 0.12 dex and 0.20 dex wide Gaussians, respectively).

An analogous map constructed using only $[Fe/H] > -1$ stars is shown in the top right panel in Figure 8. While it too displays a much stronger gradient in Z direction, a local maximum with an amplitude of $\sim$0.1 dex is discernible at $R \sim 9$ kpc and at 3–4 kpc above the plane. The $X - Y$ median metallicity map for this Z slice, shown in the lower left panel in Figure 8, places this maximum at $X \sim 10$ kpc and $Y \sim -1.5$ kpc. We address such localized metallicity inhomogeneities further below (§ 3.5).

3.4.1. The Edge of the Thick Disk Revisited

The large number of stars in DR6 sample enables a statistically robust analysis of the suspected cutoff in the distribution of thick disk stars around $|Z| \sim 5$ kpc. Figure 9 shows the metallicity distribution of $\sim$259,000 stars with $3 < R/\mathrm{kpc} < 12$ and $5 < Z/\mathrm{kpc} < 7$. When a best-fit Gaussian is subtracted from the observed distribution, a highly significant residual at $[Fe/H] > -1$ remains. This residual feature contains about 8% of stars ($\sim$21,000, so counting noise is not an issue) and suggests that, even so far away from the plane, stars with $[Fe/H] > -0.7$ are dominated by disk stars (the disk-to-halo number ratio is about 2:1). The value of 8% is in excellent agreement with the model discussed in § 3.3.4 (8.8% at $Z = 6$ kpc). An alternative interpretation is that halo metallicity distribution is not Gaussian, but skewed towards high $[Fe/H] > -1$ values, with a disk cutoff at $|Z| \lesssim 5$ kpc.

Given the remarkable agreement with a Gaussian for $[Fe/H] < -1.5$, it seems more likely that disk is indeed traceable to beyond 5 kpc from the plane.

The small peak in the observed metallicity distribution visible around $[Fe/H] = -0.5$ is probably an artifact of the photometric metallicity estimator. As discussed in § 2.3.1 and § 2.3.3, stars with $[Fe/H] > -0.5$ may be biased towards lower metallicity values, which may explain the observed (minor) effect.

3.4.2. The Metallicity–Kinematics Maps for Stars around the North Galactic Pole

Kinematic measurements can offer additional insight into Galactic components revealed by the metallicity distribution. The sky coverage of DR6 catalog includes the anticenter ($l \sim 180°$, AC hereafter) and north Galactic pole (NGP hereafter) regions where proper motion measurements provide a robust constraint on the rotational velocity component even without the knowledge of radial velocity. We take proper motion measurements from the Munn et al. (2004) catalog based on astrometric measurements from SDSS and a collection of Schmidt photographic surveys. Despite the sizable random and systematic astrometric errors in the Schmidt surveys, the combination of a long baseline (∼50 years for POSS-I survey), and a recalibration of the photographic data using positions of SDSS galaxies, results in median random errors for proper motions of only ~ 3 mas yr^{-1} for $g < 19.5$ (per component). Systematic errors are typically an order of magnitude smaller, as robustly determined using ∼80,000 spectroscopically confirmed SDSS quasars (Schneider et al. 2007). At a distance of 1 kpc, a random error of 3 mas yr^{-1} corresponds to a velocity error of ∼15 km/s, which is comparable to the radial velocity accuracy delivered by the SDSS stellar spectroscopic survey. At a distance of 7 kpc, a random error of 3 mas yr^{-1} corresponds to a velocity error of 100 km/s, which still represents a usable measurement for large samples, given that systematic errors are much smaller (∼10 km/s at a distance of 7 kpc). The faint limit of this catalog ($g \sim 20$) is well matched to the depth of SDSS photometric metallicity sample, and thus proper motion measurements are available for more than 90% of the $0.2 < g - r < 0.4$ sample. The kinematics of the SDSS stellar sample, including mutual consistency of kinematics based on radial velocity and proper motion measurements, are discussed in detail by B08. Here we briefly present a few results that are directly related to the conclusions of this paper.

For stars towards the Galactic poles, the proper motion measures the radial and rotational velocity components. We select 64,243 unresolved sources with $g < 19.5$, $0.2 < g - r < 0.4$ and $b > 80°$ from SDSS DR6. Their rotational velocity component as a function of metallicity, in three Z slices, is shown in Figure 10 (we use v_X and v_Y notation

to emphasize the spatially constrained nature of this sample, and to make a distinction from velocity components computed using a measured radial velocity; in these directions, $v_X \sim v_R$ and $v_Y \sim v_\Phi$). We do not correct velocities for solar motion relative to the local standard of rest ($v_X^\odot = -10.0 \pm 0.4$ km/s, $v_Y^\odot = -5.3 \pm 0.6$ km/s; and $v_Z^\odot = 7.2 \pm 0.4$ km/s; Dehnen & Binney 1998). Therefore, the mean value of v_Y for a non-rotating population is $v_Y = -v_Y^\odot + v_Y^{LSR} \sim 225$ km/s, where $v_Y^{LSR} \sim 220$ km/s is the rotational velocity of the local standard of rest (Gunn, Knapp & Tremaine 1979). As evident from Figure 10, the detailed behavior of the kinematics shows the same two halo and disk components as implied by the metallicity distribution. The high-metallicity disk component (selected by $[Fe/H] > -1$) lags the local rotation by 48 km/s at $Z = 1.5 - 2$ kpc and 96 km/s at $Z = 3 - 4$ kpc. The median rotational velocity for the low-metallicity subsamples selected by $[Fe/H] < -1$ is 192 km/s (top right, $Z = 3 - 4$ kpc) and 215 km/s (bottom left, $Z = 5 - 7$ kpc), with a statistical accuracy of 2 km/s for the latter. This strong metallicity-kinematic correlation is qualitatively the same as discussed in the seminal paper by Eggen, Lynden-Bell & Sandage (1962), except that here it is reproduced *in situ* with a ∼100 times larger sample, thus extending it beyond the solar neighborhood.

With the correction for solar peculiar motion, rotation of halo stars ($[Fe/H] < -1$ at $Z = 5 - 7$ kpc) indicates that the local standard of rest (LSR) is 210±10 km/s. This value scales linearly with the distance scale set by the normalization of photometric parallax relation. We used the "bright" normalization from J08, which was calibrated using *the velocity scale set by radial velocity information from the SDSS spectroscopic survey*, as discussed in detail by B08. Hence, a good agreement with the canonical LSR motion of 220 km/s (Gunn, Knapp & Tremaine 1979) implies that the halo does not rotate. The 10 km/s accuracy level of this statement is set by the systematic uncertainty in kinematic calibration of the adopted photometric parallax relation (B08).

This result is in contradiction with a claim based on similar type of analysis (proper motions and photometric parallax) by Majewski (1992) that halo counter-rotates with a speed of 55±16 km/s relative to LSR (based on proper motion measurements and photometric parallax relation for a few hundred stars towards the north Galactic pole). In order to make our v_Y for halo stars agree with Majewski's result, the distance scale given by photometric parallax relation needs to be increased by 25% (∼0.5 mag offset in absolute magnitude scale). While such an offset in photometric parallax relation would not be surprising a priori, a comparison with an independent radial velocity scale rules out such a large error (B08). In addition, Carollo et al. (2007) claim that the inner halo ($\lesssim$10 kpc) shows a modest prograde rotation (0-50 km/s).

3.4.3. A Model for the Rotational Velocity Distribution

The marginal rotational velocity distributions for maps from Figure 10 are shown in Figure 11 (assuming $v_Y = v_\Phi$). Analogously to modeling the metallicity distributions in § 3.3.1, we first attempt to fit the dependence of rotational velocity distribution on distance from the Galactic plane, Z, using a Gaussian for the halo component and a universal shape, modeled as two coupled Gaussians, for the disk component (an alternative approach based on thin/thick disk decomposition is described below).

We heuristically model the *shape* of the disk velocity distribution as a sum of two Gaussians with fixed positions relative to each other (offset of 45 km/s), fixed widths (18 km/s and 42 km/s), and fixed relative normalization (1-to-1 number ratio). The central velocity of the narrower Gaussian is fit as a linear function

$$v_n(Z) = -6.0 + 19.2\,|Z/\mathrm{kpc}| \ \mathrm{km/s}, \tag{14}$$

such that the disk stars show increasing rotational lag with increasing height above the plane. The values of these six free parameters were obtained by *simultaneously* fitting the four histograms shown in Figure 11. The halo velocity distribution was kept fixed as a Gaussian centered on 215 km/s and with a width of 100 km/s, and the fractional contribution of halo stars was computed using eq. 8. In each Z bin, the expected velocity measurement error was added in quadrature to the widths of all three Gaussians. The velocity error was computed using the median distance of all stars in the bin, and a proper motion error of 3 mas/yr per coordinate. The best-fit parameters are listed in Table 4 and the best fits are shown in Figure 11. As evident, this simple model of a skewed distribution that slides linearly with Z provides a satisfactory description of the data.

For the adopted double-Gaussian velocity distribution, the mean at each Z is equal to $v_n(Z) + 23$ km/s, and the median is $v_n(Z) + 15$ km/s. The intrinsic rms scatter (computed from interquartile range for a large Monte Carlo sample) is 41 km/s. The observed increase of the rotational velocity dispersion of disk stars with Z is fully consistent with the increase of measurement errors (the velocity errors increase linearly with distance from ∼10 km/s to ∼100 km/s, see the last column in Table 4). It is remarkable that the data admit a spatially invariant intrinsic velocity dispersion for the disk component.

The decrease of rotational velocity with Z (sometimes called velocity lag) was first convincingly detected by Majewski (1992), using photographic data for 250 stars. At $Z \sim 1.5 - 2.0$ kpc, he found a lag of 50±10 km/s, in good agreement with the value of 50.6 km/s given by eq. 14 (recall that the *mean* lag is $v_n + 23$ km/s). Chiba & Beers (2000) measured somewhat steeper gradient of 30±3 km/s/kpc. Using proper motion data for about a million M dwarfs, Ivezić et al. (2005) reported essentially the same behavior of rotational velocity

at $Z < 1$ kpc, with a median value of 34 km/s at $Z = 1$ kpc, which agrees well with the lag of 36 km/s obtained here using F dwarfs. Using SDSS radial velocity data, Allende Prieto et al. (2006) measured a vertical rotational velocity gradient of 16 km/s, which is similar to the results based on proper motion measurements. Most recently, Girard et al. (2006) used data for 1200 red giants and detected "velocity shear" towards the south galactic pole. The mean velocity gradient of 19.2 km/s/kpc given by eq. 14 is smaller than their value of 30±3 km/s/kpc. They also detected a vertical gradient in the rotational velocity dispersion of (10±3) km/s/kpc. These $\sim 3\sigma$ discrepancies may be due to different tracers, analysis methods, or north-south asymmetry. We note that their detection of a velocity dispersion gradient could be due to underestimating proper motion errors by about 10%. Despite this detailed disagreement, overall the results presented here and those from Girard et al. (2006) are remarkably consistent.

We use the best fits for the marginal metallicity distribution described in § 3.3.1 (see Figure 7), and the best fits for marginal rotational velocity distribution discussed above to model the observed joint distributions in the rotational velocity vs. metallicity plane, shown in Figure 10. In each Z bin, we simply multiply the best-fit marginal distributions and subtract their product from the observed map. There are two important assumptions underlying this approach: the disk and halo components used to model the two marginal distributions map well onto each other, and the velocity and metallicity distributions of each individual component are uncorrelated.

These assumptions are borne out by the data. As an illustration of the residual and χ^2 maps, we show the $Z = 3 - 4$ kpc bin, which contains similar fractions of disk and halo stars (Figure 12). The observed distribution is successfully modeled to within expected statistical noise ($\sim$30% for counts per pixel, on average). The observed lack of a correlation between velocity and metallicity distributions for disk component is at odds with traditional thin/thick disk decomposition, which we address next.

3.4.4. Difficulties with the Thin–Thick Disk Separation?

Our model fits above show that the data for both metallicity and rotational velocity distributions of disk stars can be fit with shapes that do not vary with Z. While formally these skewed distributions are modeled as sums of two Gaussians, these Gaussians cannot be readily identified with the classical thin and thick disks. First, their normalization ratio is constant, while double-exponential best-fit to the observed spatial profile predicts that the fraction of stars in each component should strongly vary with Z. Second, the normalization ratios are *different*, 1.7 for metallicity distributions and 1.0 for rotational velocity

distributions, which implies that the two components do not perfectly map onto each other.

Despite these difficulties, it is instructive to attempt traditional thin plus thick disk decomposition using the data presented here. We seek metallicity and velocity distributions whose linear combination, with weights given by the observed spatial profiles, reproduces the variation of observed distributions with Z. This can be done with only a minimal reliance on models because the data span a wide range of Z, *and because there are clearly detected Z gradients in both metallicity and velocity distributions, that cannot be attributed to halo stars*. The disk spatial profile (with J08 best-fit parameters) implies that $|Z| = 2.0-2.5$ kpc bin is dominated by thick disk stars (with a 38% contribution from halo stars), while they contribute ∼60%, ∼70% and ∼90% of all disk stars in $|Z| = 0.5 - 1.0$ kpc, $|Z| = 1.0 - 1.25$ kpc, and $|Z| = 1.5 - 2.0$ kpc bins, respectively. Therefore, one can subtract the ∼38% halo contribution from the metallicity distribution in $|Z| = 2.0 - 2.5$ kpc bin, re-normalize the difference, and treat it as the thick disk metallicity distribution. It can be subtracted, after renormalization, from the disk-dominated metallicity distribution in the $|Z| = 0.5 - 1.0$ kpc bin. The renormalized difference can be treated as a pure thin disk distribution. The two distributions can then be linearly combined and compared to distributions observed in the two intermediate bins.

The top left panel in Figure 13 shows the result of this comparison for the $|Z| = 1.0-1.25$ kpc bin. The metallicity distributions for both components appear non-Gaussian, with a difference of their means of about 0.2 dex. Their expected linear combination reveals discrepancies with the data, but they are not overwhelming and could be due to uncertainties in the decomposition procedure itself.

A similar linear decomposition method cannot be applied to kinematic data analyzed here because the velocity measurement errors increase too much over the relevant range of Z. Instead, we choose to model the observed velocity distributions using two Gaussians, with fixed mean velocities and dispersions. The widths are convolved with known, Z-dependent, velocity measurement errors when fitting the four free parameters. We first attempted to normalize the two Gaussians assuming their relative contributions (and halo normalization) predicted by the density (counts) profiles shown in Figure 6. This approach resulted in poor agreement with the data. We then relaxed this assumption and allowed the relative normalization for all three components to be free.

The best-fits are shown in Figure 13 for three representative Z bins, with the best-fit parameters listed in Table 5. The best-fit values of the thick-to-thin disk number ratio are significantly different than predicted from the counts profiles, which by itself is a major problem. The presumed thick disk Gaussian has a velocity lag of 48 km/s, relative to the first Gaussian (centered at 57 km/s and 9 km/s, respectively). The implied velocity dispersions

are 18 km/s and 28 km/s. The fits are not as good as those shown in Figure 11, but the discrepancies are not overwhelming. They are formally highly statistically significant due to a large number of stars, but there is always a possibility for hidden systematic errors. If the thick-disk Gaussian were replaced by a non-Gaussian velocity distribution, it is likely that the most egregious discrepancies around $v_\Phi \sim 150$ km/s could be resolved.

Therefore, the marginal metallicity and velocity distributions do *not* strongly rule out the thin/thick disk linear combination hypothesis, but *only if* both disks have non-Gaussian metallicity and velocity distributions (and ignoring discrepancy between best-fit normalization and that implied by counts profile). The choice for both metallicity and rotational velocity distributions is then between a linear combination of two fixed non-Gaussian distributions, or a single non-Gaussian distribution that slides with Z. A difficulty with the former hypothesis is that the implied thin disk metallicity distribution has a mean of about -0.6, which is too metal poor by about 0.4 dex, compared to local measurements (Girardi & Salaris 2001; Nordström et al. 2004). On the other hand, there is a worrisome possibility of a metallicity "compression" discussed in Appendix B, which could bias thin disk measurements to lower values.

While fitting the marginal metallicity and kinematic distributions separately does not strongly discriminate among models, the thin/thick disk linear combination hypothesis makes a very strong prediction about the joint two-dimensional distribution. Because the individual components are offset by ∼0.2 dex in metallicity, and by ∼50 km/s in rotational velocity, this hypothesis predicts a correlation between metallicity and rotational velocity for samples selected from narrow Z slices in the Z range where neither component dominates. To compute the strength of this correlation, we generated a Monte Carlo sample for $Z = 1.0 - 1.25$ kpc bin, where the correlation should be strong, with the same size as the observed sample. The distributions of the data and model stars in the velocity vs. metallicity plane are shown in Figure 14.

Even without any computation, it is evident from the lower left panel in Figure 14 that the model distributions are strongly correlated. The value of Kendall's rank correlation coefficient (e.g., see Lupton 1993) for the model distribution is -0.30 ± 0.04, which is significantly inconsistent with the observed value of -0.015 ± 0.018 (we limit velocities to 120 km/s, and metallicity to $[Fe/H] > -1$ to exclude halo stars).

In order to test whether this observed lack of correlation is localized to the north Galactic pole, we have also evaluated the Kendall's rank correlation coefficient for stars with $Z = 1.0 - 1.25$ kpc in three 10 degree wide patches along the $l = 180°$ line and with b=50°, 30°, and −50°. None of these patches shows a statistically significant correlation between velocity and metallicity, with the value of correlation coefficient towards the north Galactic pole remaining

the most negative. In order to test whether the measured correlation coefficient depends on the selection of Z bin, we evaluated it for seven 200 pc thick bins in the range Z=0.5–2.1 kpc, and found values statistically consistent with the value for $Z = 1.0 - 1.25$ kpc bin.

As yet another statistics, that is less sensitive to errors in adopted metallicity scale, we compared velocity histograms for stars with $-1 < [Fe/H] < -0.8$ and $-0.6 < [Fe/H] < -0.4$. The observed median rotation velocities differ by 1 km/s, while the model values differ by 25 km/s, or eight times more than expected statistical noise. We conclude that *the absence of a correlation between the observed velocity and metallicity distributions for disk stars represents a major problem for the interpretation of vertical velocity and metallicity gradients as being due to a varying linear combination of two fixed distributions.*

Our conclusion does not contradict previous work on this subject because the older samples did not include *simultaneous* distance, velocity and metallicity measurements for a sufficient number of stars with appropriate distance distribution. A test based on a randomly selected ten times smaller subsample, with photometric errors and proper motion errors increased by a factor of two, resulted in an inconclusive difference in Kendall's correlation coefficients between the "data" and a thin/thick disk model.

It is noteworthy that Norris (1987) proposed a Galaxy model which does not assume that thin and thick disks are discrete components, but instead form a kinematical and chemical continuum. Stars traditionally associated with the thick disk belong to an "extended" disk (in terms of spatial distribution) in Norris' terminology and represent an extreme tail of metallicity and kinematic distributions. Our results appear roughly consistent with Norris' proposal and provide a quantitative support for such "continuous" view of the disk over the entire relevant range of distances from the Galactic plane.

3.4.5. A Kinematic Estimate of the Effect of Metallicity on Photometric Parallax Relation

The dependence of photometric parallax on metallicity could bias our results, and here we estimate the importance of this effect using indirect kinematic constraints. We select ∼10,000 stars with $b > 80$ and $5 < Z/\mathrm{kpc} < 7$, and compute the median v_Y in 0.1 dex wide metallicity bins in the range $-2.1 < [Fe/H] < -0.5$. The medians are well described by

$$\langle v_Y \rangle = 220 - 66([Fe/H] + 1.50) \text{ km/s}, \quad (15)$$

with a scatter around this relation, of ∼5 km/s, consistent with statistical noise. Only the most metal-rich bin has a larger deviation (the median is 128 km/s, instead of 154 km/s predicted by the above expression). This relation is shown by the dashed line in the bottom right panel in Figure 10.

While it is possible that halo kinematics could depend on stellar metallicity, this behavior is consistent with the expected effect of metallicity on photometric parallax relation. If absolute magnitudes given by eq. 1 are corrected using eq. 9, the dependence of the median v_Y on metallicity disappears. The gradient $dM_r/d[Fe/H] = -0.75$ (metal-rich stars are more luminous at a given T_{eff}) is somewhat smaller than given by Laird, Carney & Latham (1988), but this is expected due to bandpass difference (Reid et al. 2001). After applying this correction, the median v_Y for stars with $-0.6 < [Fe/H] < -0.4$ and $5 < Z/\mathrm{kpc} < 7$ becomes 178±10 km/s (statistical uncertainty only), corresponding to a median increase of distance scale by 38%, while the median v_Y for stars with $[Fe/H] < -1.0$ changes from 216 km/s to 219 km/s (with statistical errors of 2 km/s) for the same distance range.

We chose *not* to apply this correction in our analysis because it is not determined by a direct measurement but is based instead on a conjecture that the median rotational velocity of halo stars does not depend on metallicity. Also, it is not obvious that it is valid at the metal-rich end of the sample[15]. Nevertheless, since it appears quite plausible and consistent with expectations, we have repeated the entire analysis with distances corrected for the presumed metallicity effect. The impact on halo kinematics is minor, while the increase in velocities of disk stars varies from ∼20% at $[Fe/H] = -1$ to ∼40% at $[Fe/H] = -0.5$. As a result of this correction, the maps analogous to those shown in Figure 10 are stretched vertically by these metallicity-dependent factors. The impact on the conditional metallicity distribution was already discussed in § 3.3.2.

3.4.6. The "Metal-weak Thick Disk" Revisited

In order to test whether the third Gaussian component discussed in § 3.3.1 has the same kinematics as the rest of disk stars, we compare the v_Y histograms for $-1.1 < [Fe/H] < -0.8$ and $-0.6 < [Fe/H] < -0.5$ subsamples in two Z bins: 0.5–1 kpc and 1.5-2.0. We find no statistically significant differences, with an upper limit on the relative velocity offset of ∼15 km/s. This kinematic similarity supports the view that stars with $-1.1 < [Fe/H] < -0.8$ reflect a non-Gaussian metallicity distribution of disk stars, rather than a separate entity (Beers et al. 2002).

---

[15]The g vs. $g-r$ color-magnitude diagrams for clusters M2 ($[Fe/H] = -1.62$) and NGC 2420 ($[Fe/H] = -0.44$) presented by Lee et al. (2007b) suggest that offsets in their absolute magnitudes evaluated at $g-r = 0.4$ are consistent with eq. 9. However, no detectable offset (<0.1 mag) is found between absolute magnitudes for NGC 2420 and M67 ($[Fe/H] = 0.02$) evaluated at $g-r = 0.8$.

3.5. Spatially Localized Deviations from the Mean Metallicity Distribution

The rich metallicity and kinematic data presented here enable more powerful searching for the Milky Way substructure than possible using the stellar number density maps alone. We utilize the large sky coverage of DR6 catalog to quantify spatial deviations from the conditional metallicity distribution discussed in § 3.2 and 3.3. We first constructed 51 maps, such as that shown in the top right panel in Figure 5, for regions defined by a 1 kpc by 1 kpc square footprint in the $X - Y$ plane. In each map, we compute the median metallicity in two Z slices that are dominated by disk (1–2 kpc) and halo (5–7 kpc) stars. The range of cylindrical radius, R, is 6–14 kpc for the disk slice, and 5–15 kpc for the halo slice.

In the range $6 < R/\mathrm{kpc} < 10$, the median disk metallicity is $[Fe/H] = -0.72$, with an rms scatter of 0.05 dex, and the median distribution width of 0.27 dex. There is no discernible radial metallicity gradient, with an upper limit of 0.01 dex/kpc. For $R > 10$ kpc, the median metallicity is $[Fe/H] = -0.80$, with the shift of 0.08 dex probably due to stars from the Monoceros stream, as discussed below. The median halo metallicity is $[Fe/H] = -1.40$, with an rms scatter of 0.03 dex, and the median distribution width of 0.41 dex. There is no discernible radial metallicity gradient, with an upper limit of 0.005 dex/kpc.

The mean expected statistical scatter in the medians is 0.005 dex for disk and 0.011 for halo (wider distribution and fewer stars for the latter), suggesting that the variation of the median halo metallicity is probably insignificant, while the rms variation of the median disk metallicity of 0.05 dex appears real. The photometric calibration errors in individual SDSS runs, which could produce a metallicity scatter of a similar magnitude, are averaged out because many runs contribute to each map. Furthermore, such an instrumental effect is ruled out by the fact that the u band calibration errors would have to have an rms of 0.02 mag to produce the disk median metallicity rms of 0.05 dex, and only 0.006 mag to produce the halo rms of 0.03 dex. Hence, were the disk rms due to calibration errors, the halo rms would have been 0.1 dex, and not 0.03 dex.

As an additional method to search for localized substructure, we subtracted a best-fit model from each map (such as those described in § 3.3), and visually inspected residual maps. The only strong feature found in residual maps was localized at $Y \sim 0$, $Z \sim 3 - 4$ kpc and $R \sim 15$ kpc, and represents an excess of $[Fe/H] \sim -1$ stars. It is clearly visible in the median metallicity RZ map and, as an especially striking feature, in a conditional metallicity distribution map shown in Figure 15. Using its spatial position, we identify this

feature as the Monoceros stream[16] discovered in SDSS data using stellar counts by Newberg et al. (2002).

3.5.1. The Metallicity Distribution for the Monoceros Stream

The conditional metallicity map from Figure 15 demonstrates that regions with $R < 12$ are not strongly affected by the Monoceros stream. We compare the metallicity distributions for stars with $6 < R/\mathrm{kpc} < 9$ (control sample), and for stars with $13 < R/\mathrm{kpc} < 16$, in the two bottom panels in Figure 15. The metallicity distribution of the control sample is consistent with the halo and disk metallicity distributions described in § 3.3.1, with a few minor adjustments: the disk distribution is shifted by 0.07 dex, and the halo distribution by 0.02 dex, towards higher metallicity, the fraction of halo stars is changed from 61% to 55%, and 0.16 dex is added in quadrature to the widths of the three Gaussians to account for increased metallicity errors in single-epoch DR6 data.

The subsample containing the Monoceros stream can be described using the same function as for the control sample, and an additional 0.22 dex wide Gaussian component centered on $[Fe/H] = -0.96$, and with a relative normalization of 37%. When corrected for measurement errors, the implied width of the metallicity distribution for the Monoceros stream is 0.15 dex. The best-fit normalization is in good agreement with spatial profiles from J08, which suggests that the Monoceros stream is about a factor of 2 overdensity over the local background counts (i.e. a relative normalization of 50%).

3.5.2. The Kinematics of the Monoceros Stream

We select a subsample of ∼11,000 stars that maximizes the fraction of stars from the Monoceros stream, and allows an estimate of rotational velocity using only longitudinal proper motion, by requiring $|Y| < 1$ kpc, $3 < Z/\mathrm{kpc} < 4$, $13 < R/\mathrm{kpc} < 16$ and $170^\circ < l < 190^\circ$. The distribution of these stars in the rotational velocity vs. metallicity diagram is shown in the top right panel in Figure 16. It is discernible that the Monoceros stream has kinematics more similar to disk stars than to halo stars. We obtain a more accurate assessment with the aid of an analogous map for a control sample selected using similar

[16]Immediately following its discovery, it was not clear whether the Monoceros stellar overdensity was a ring, stream or due to disk flaring. Subsequent work has demonstrated its stream-like profile, see, e.g., maps in J08.

criteria, except that $9 < R/\mathrm{kpc} < 12$ (top left panel). The difference of these two maps is shown in the bottom left panel.

The excess stars are centered on $[Fe/H] \sim -1$, as expected from the best-fit described above. Their velocity distribution shows a strong peak at $v_l \sim v_\Phi \sim -50$ km/s, with a long tail towards more positive velocities. This residual map indicates that most of the Monoceros stream stars move in the direction of LSR rotation with velocities of up to ∼270 km/s. This result is qualitatively in agreement with Penarrubia et al. (2005), who ruled out retrograde motions using models and proper motion measurements.

The latitudinal velocity, v_b, based on latitudinal proper motion component, is a linear combination of radial and vertical velocity components. The median latitudinal velocity of stars from the Monoceros stream region in the rotational velocity vs. metallicity plane is shown in the bottom right panel in Figure 16. There is no significant offset from 0 (< 20 km/s) in parts of the diagram where the excess of the Monoceros stream stars is the highest. This presumably indicates that contributions from the radial and vertical motion for the Monoceros stream stars cancel (for disk stars, the medians for both components should be 0). Together with radial velocity measurements obtained by Conn et al. (2005) and Martin et al. (2006), this information can be used to further refine models, such as those described by Penarrubia et al. (2005).

4. Discussion and Conclusions

The spectroscopic stellar parameters for over 60,000 F and G dwarfs, computed by the SEGUE Stellar Parameters Pipeline (Beers et al. 2006; Allende Prieto et al. 2006, 2007; Lee et al. 2007ab) using the SDSS spectroscopic database, allowed us to derive photometric estimators for effective temperature and metallicity in the SDSS photometric system. The availability of the SDSS imaging survey, with its accurate ugr photometry, then enabled an unbiased volume-limited study of the stellar metallicity distribution to a distance limit of ∼10 kpc.

4.1. Photometric Estimates for Effective Temperature and Metallicity

The photometric metallicity estimator based on the SDSS $u - g$ and $g - r$ colors is reminiscent of the traditional δ method based on the UBV photometry. It reflects the same physics and can be applied to F and G type main sequence stars ($0.2 < g - r < 0.6$). For the SDSS single-epoch main survey data, it provides metallicity accurate to 0.2 dex

or better for stars brighter than about $g = 19.5$. In this magnitude and color range, the photometric effective temperature estimator reproduces spectroscopic temperature with a root-mean-square scatter of only ∼100 K. The accuracy[17] of 100 K for effective temperature, and 0.2 dex or better for metallicity, are comparable to parameter accuracy achieved using artificial neural networks with spectroscopic observations (Snider et al. 2001), and the estimated accuracy of parameters determined from SDSS spectra (Beers et al. 2007). It is plausible that increased photometric accuracy would further improve these values. For example, photometry accurate to 1% may enable MK spectral type determination with errors smaller than one subtype. Derived mapping from color space to metallicity implies that, at least formally, an error in the $u - g$ color of 0.01 mag induces a metallicity error that varies from 0.01 dex at $[Fe/H] = -0.5$ to 0.06 dex at $[Fe/H] = -1.5$. This is as good a performance as obtained by the Strömgren $uvby\beta$ narrow-band photometric system which was optimized for this purpose (e.g., Strömgren 1966; Nordström et al. 2004). In other words, the increase of metallicity errors due to increased bandpass width can be compensated for by an improved photometric accuracy.

We apply these methods to a photometric catalog of coadded SDSS observations from the so-called Stripe 82 (Ivezić et al. 2007). These deeper and photometrically exceedingly precise coadded data allowed us to measure an unbiased metallicity distribution for a *volume limited sample* of ∼200,000 F and G type stars in the 0.5–8 kpc distance range. We also study metallicity distribution using a shallower but much larger sample of several million stars in 8500 sq. deg. of sky provided by SDSS Data Release 6. The large sky coverage tests the conclusions derived using the relatively small Stripe 82 sample and enables detection of coherent substructures in the kinematics–metallicity space, such as the Monoceros stream.

4.2. The Milky Way Structure and Multi-dimensional Stellar Counts

From an observer's point of view, the ultimate goal of the Milky way studies is to measure and describe the distribution (counts) of stars in the space spanned by apparent brightness, colors in multiple bandpasses[18], two proper motion components (μ_l, μ_b), radial

[17]Here, precision may be a more appropriate terminology than accuracy because the photometric estimates are tied to SDSS spectroscopic values rather than to an absolute metallicity scale. That is, all systematic errors in SDSS spectroscopic parameters are inherited by photometric estimators.

[18]We limit this analysis to two colors, $u-g$ and $g-r$, which provide good estimates of effective temperature and metallicity for F and G main sequence stars. However, an alternative is to consider a full spectral shape, instead of colors, which carries all the relevant information about the three main stellar parameters (T_{eff}, $[Fe/H]$, $log(g)$).

velocity (v_{rad}), and position on the sky. Specialized to SDSS data, we seek to understand the 8-dimensional probability density function, $p(g, u-g, g-r, \mu_l, \mu_b, v_{rad}, l, b)$. This function could be described empirically, without any reference to stellar and Galactic structure, but in practice measurements are used to place constraints on the latter. From a theorist's point of view, the problem of interpreting data can be rephrased as: given a small control volume centered on (R, Z, ϕ),

- what is the distribution of stars as a function of luminosity[19], L,
- what is the metallicity distribution for a given L, and
- what are the distributions of 3 velocity components, v_ϕ, v_R and v_Z, for a given L and metallicity?

Guided by these questions, we can write

$$p(g, u-g, g-r, \mu_l, \mu_b, v_{rad}, l, b) = p(g, g-r|l, b)\, p(u-g|g, g-r, l, b)\, p(\mu_l, \mu_b, v_{rad}|u-g, g, g-r, l, b), \quad (16)$$

where the three functions on the right side of eq. 16 are discussed in this and two companion papers:

1. The function $p(g, g-r|l, b)$ describes the behavior of the g vs. $g-r$ color-magnitude (Hess) diagram as a function of position on the sky. This behavior is a reflection of stellar luminosity function, $\Phi(L)$, and the dependence of stellar number density on spatial coordinates, $\rho(R, Z, \phi)$. A best-fit model for $\rho(R, Z, \phi)$ developed by J08 is discussed in § 3.3.4.

2. The function $p(u-g|g, g-r, l, b)$ describes the $u-g$ color distribution for a given bin in the g vs. $g-r$ color-magnitude diagram, and as a function of position on the sky. The $u-g$ color distribution reflects the metallicity distribution, $p([Fe/H]|R, Z, \phi)$, and $\rho(R, Z, \phi)$. In this contribution, we show that, similarly to $\rho(R, Z, \phi)$, $p([Fe/H]|R, Z, \phi)$ can be well described (apart from local overdensities) as a sum of two components

$$p(x = [Fe/H]|R, Z, \phi) = [1 - f_H(R, Z)]\, p_D(x|Z) + f_H(R, Z)\, p_H(x), \quad (17)$$

where the halo-to-disk counts ratio is simply $f_H(R, Z) = \rho_H(R, Z)/[\rho_D(R, Z) + \rho_H(R, Z)]$.

[19]At least in principle, it would be desirable to measure stellar luminosity function, and other quantities, as a function of stellar age, but estimating age for individual stars is very difficult (e.g., Nordström et al. 2004; Jorgensen & Lindegren 2005) and beyond the scope of this paper.

The halo metallicity distribution, $p_H([Fe/H])$, can be modeled as a spatially invariant Gaussian centered on $[Fe/H] = -1.46$ (for Stripe 82 catalog; for the full DR6 sample, the median [Fe/H]=−1.40) and with the intrinsic (not including measurement errors) width $\sigma_H = 0.29$ dex. For $|Z| \lesssim 10$ kpc, an upper limit on the halo radial metallicity gradient is 0.005 dex/kpc.

The metallicity distribution of disk component has an rms scatter of 0.16 dex, and the median varying as

$$\mu_D(Z) = -0.78 + 0.35 \exp(-|Z|/1.0\,\mathrm{kpc}) \text{ dex}, \tag{18}$$

at $|Z| > 0.5$ kpc. In the $|Z| = 1.0 - 1.5$ kpc range, the median metallicity is consistent with the measurements by Gilmore & Wyse (1995). For $|Z| \lesssim 5$ kpc, an upper limit on the disk radial metallicity gradient is 0.010 dex/kpc. The *shape* of the metallicity distribution of disk component is non-Gaussian and can be modeled as

$$p_D(x = [Fe/H]|Z) = 1.7\, G[x|\mu = a(Z), \sigma = 0.20] + G[x|\mu = a(Z) + 0.1, \sigma = 0.10], \tag{19}$$

where the position a and the median μ_D are related via $a(Z) = \mu_D(Z) - 0.067$ (unless measurement errors are very large). These results represent powerful new constraints for the Galaxy formation and chemical evolution models (e.g., Tinsley 1975; Pagel & Patchett 1975; Wyse & Gilmore 1995; and references therein).

3. The function $p(\mu_l, \mu_b, v_{rad}|u-g, g, g-r, l, b)$ describes proper motion and radial velocity measurements for a given bin in the g vs. $g-r$ color-magnitude, as a function of position on the sky, and as a function of the $u-g$ color. This function locally reflects the behavior of the velocity ellipsoid, but SDSS data probe sufficiently large distances to detect its spatial variation, as discussed in detail by B08. They find that the detailed behavior of kinematics can also be well described (apart from local overdensities) as a sum of two components, disk and halo, that map well to components detected in spatial profiles and metallicity distribution. The non-rotating halo component has by and large spatially uniform kinematics (in an overall sense, e.g., B08 discuss several kinematically coherent structures), while the disk kinematics are dominated by a vertical (Z) gradient. The mean rotational velocity and the three velocity dispersions for disk stars can be modeled as relatively simple functions of the form $a + b|Z|^c$, as discussed in detail by B08 (see also Girard et al. 2006). The shape of the rotational velocity distribution for disk component is non-Gaussian and can be modeled, in the $|Z| = 0.5 - 5.0$ kpc range (and $R \sim 8$ kpc), as

$$p_D(x = v_\Phi|Z) = G[x|\mu = v_n(Z), \sigma = 18] + G[x|\mu = v_n(Z) + 45, \sigma = 42], \tag{20}$$

where

$$v_n(Z) = -6 + 19.2\,|Z/\mathrm{kpc}| \ \ \mathrm{km/s}. \tag{21}$$

We reiterate that the widths listed for $p_D([Fe/H]|Z)$ and $p_D(v_\Phi|Z)$ are *intrinsic* widths and *have to be convolved with measurement errors when comparing to observations.* The listed widths are measured with a relative accuracy of ∼10%.

These functions provide a good description of the overall features in the distribution of stars in the spatial-kinematic-metallicity space, as observed by SDSS. Qualitatively, these results are in fair agreement with previous work (e.g., Gilmore & Wyse 1985; Gilmore, Wyse & Kuijken 1989; Majewski 1993; Nordström et al. 2004; Girard et al. 2006). Quantitatively, the availability of SDSS data is enabling unprecedentedly powerful and robust studies, not only due to large volume, but also thanks to accurate and diverse measurements. In particular, with the SDSS data, the reach of massive statistical studies can now be extended from < 100 pc HIPPARCOS's distance limit (e.g., Dehnen & Binney 1998; Nordström et al. 2004) to ∼10 kpc.

The results presented here are only a brief illustration of the great scientific potential of the SDSS stellar spectroscopic database. This dataset will remain a cutting edge resource for a long time because other major ongoing and upcoming stellar spectroscopic surveys are either shallower (e.g., RAVE, $9 < I < 12$), or have a significantly narrower wavelength coverage (GAIA).

4.2.1. Is there a thick disk?

Perhaps the most significant result of our study, in addition to detection of abundant substructure in metallicity space, is that transition from the thin to the thick disk, seen (and originally defined by Gilmore and Reid, 1983) as an abrupt change of slope in the log(counts) vs. Z plot around $|Z| \sim 1$ kpc, can be modeled as smooth shifts of metallicity and velocity distributions that do not change their shape. More quantitatively, using the above notation, the disk metallicity and velocity distribution can be described as

$$p_D(x = v_\Phi \,\mathrm{or}\, [Fe/H]|Z) = n_1(Z)\, G[x|\mu_1(Z), \sigma_1] + n_2(Z)\, G[x|\mu_2(Z), \sigma_2]. \tag{22}$$

Traditionally, the two components are interpreted as thin and thick disks, and $n_1(Z)$ and $n_2(Z)$ are constrained by stellar number counts. They are modeled as exponential functions with scale heights of ∼300 pc and ∼1000 pc, with $\mu_1(Z)$ and $\mu_2(Z)$ typically assumed independent of Z. This description is only mildly inconsistent with observed *marginal* metallicity and velocity distributions. However, when the two distributions are analyzed *simultaneously*,

this decomposition faces a serious difficulty. Because it combines *different* metallicity and velocity distributions for thin and thick disk components (data require offsets of 0.2 dex and 45 km/s), it predicts a strong and detectable correlation between them. The data presented here do not display any significant correlation, and rule out this prediction at a highly significant level ($\sim 8\sigma$).

We find an alternative interpretation that does not imply a strong correlation between metallicity and velocity distributions. Formally, we find that the data can be fit with n_1 and n_2 that do not vary with Z (eqs. 19 and 20), while μ_1 and μ_2 are *coupled* and vary with Z according to eqs. 18 and 21. This ability to describe the disk metallicity and velocity distributions using functions with universal Z-independent shapes has fundamental implications for its origin: instead of two distinct components, our data can be interpreted with a single disk, albeit with metallicity and velocity distributions more complex than a Gaussian (but the data require non-Gaussian distributions even in traditional interpretation). While the disk separation into thin and thick components may still be a useful concept to describe the fairly abrupt change of number density around $|Z| \sim 1$ kpc (which is detected beyond doubt, see J08 for SDSS results), the disk spatial profile may simply indicate a complex structure (i.e. not a single exponential function), rather than two distinct entities with different formation and evolution history. If this is correct, then our results imply that *different processes led to the observed metallicity and velocity distributions of disk stars,* rather than a single process, such as mergers or an increase of velocity dispersion due to scattering, that shaped both distributions.

On the other hand, it appears that stars from the solar neighborhood, believed to be thick disk stars because of their *kinematic* behavior, have larger α element abundances, at the same $[Fe/H]$, than do thin disk stars (e.g., Fuhrmann 2004; Bensby et al. 2004; Feltzing 2006; Reddy et al. 2006; Ramírez et al. 2007). The thick disk stars, again selected kinematically, appear older than the thin disk stars (e.g., Fuhrmann 2004; Bensby et al. 2004). Thus, it is possible that the data presented here are insufficient to distinguish detailed elemental and age differences, and that high-resolution spectroscopy is required to do so. If such supplemental data were available, for example, for ∼20,000 stars analyzed in Figures 7 and 11, one could determine whether the distributions of individual α elements admit a universal shape, and whether they are *correlated with kinematics*. These stars are confined to several hundred sq.deg. of sky, with a sky density of ∼100 deg^{-2}, and those at $|Z| < 4$ kpc have $g \lesssim 18$. Such an undertaking is within the reach of modern spectrographs installed on 10m-class telescopes.

4.2.2. Multidimensional Substructure

The samples discussed here are sufficiently large to constrain the global behavior of metallicity distribution and to search for anomalies. The halo metallicity distribution is remarkably uniform. The rms scatter in the median value for 2 kpc^3 large bins of only 0.03 dex is consistent with expected statistical noise. The median disk metallicity in 1 kpc^3 large bins in the $Z = 1 - 2$ kpc range shows a statistically significant, but still fairly small rms scatter of 0.05 dex. We detect a vertical metallicity gradient for disk stars (0.1–0.2 dex/kpc), but radial gradients are limited to $\lesssim$0.01 dex/kpc for both disk and halo components, outside of regions with strong substructure.

The strongest overdensity identified in the metallicity space is the Monoceros stream. Its metallicity distribution is distinct from those for both halo and disk, and has a similar width as the metallicity distribution of disk stars ($\sim$0.15 dex). Hence, recent discoveries of abundant substructure in stellar spatial distribution and kinematics are now extended to metallicity space. We concur with Nordström et al. (2004) that "the Galaxy is a far more complicated and interesting subject than ever before".

4.2.3. The Implications for Future Imaging Surveys

The analysis and conclusions presented here are relevant for upcoming large-scale deep optical surveys such as the Dark Energy Survey (Flaugher et al. 2007), Pan-STARRS (Kaiser 2002) and the Large Synoptic Survey Telescope (Tyson 2002, LSST hereafter). Of those, only LSST plans to obtain data in the u band[20]. Over its 10-year long lifetime, the LSST survey will obtain about 60 observations in the u band of a 20,000 deg^2 large area. Thanks to its large aperture, the median 5σ depth of $\sim$ 24 (for point sources) will be significantly fainter than for SDSS data (22.5), and the coadded data will reach a 5σ depth of $u = 26$. The potential of photometric metallicity estimator for studying the evolution and structure of the Milky Way demonstrated here bodes well for LSST science mission.

Using SDSS data, we estimate the number of stars for which LSST will provide metallicity measurements. Based on the discussion presented in §2, we adopt an error in the $u - g$ color of 0.05 mag as a practical limit for robust metallicity studies. This color error corresponds to a metallicity error of 0.1 dex for metal-rich stars, and 0.2 dex for metal-poor stars. The LSST data will achieve this color accuracy for stars with $0.2 < g - r < 0.6$ if $g < 23.5$. This is about 4 magnitudes deeper than the analogous limit for SDSS survey. Based on

[20]The LSST science requirements document is available from http://www.lsst.org/Science/lsst_baseline.shtml

the counts of SDSS stars, we estimate that LSST will measure metallicity accurate to 0.2 dex or better[21] for at least 200 million F/G main sequence stars brighter than $g = 23.5$ (without accounting for the fact that stellar counts greatly increase close to the Galactic plane). For these stars[22], LSST will also provide proper motion measurements accurate to about 0.2 mas/yr at $g = 21$ and 0.5 mas/yr at $g = 23$ (about 10 times more accurate and ∼3 magnitudes deeper than the SDSS-POSS catalog by Munn et al. used in this work). This data set will represent a deep complement to the GAIA mission ($g \lesssim 20$; Perryman et al. 2001; Wilkinson et al. 2005), and will enable detailed exploration of the Milky Way halo in a six-dimensional space spanned by three spatial coordinates, two velocity components and metallicity, within a distance limit of ∼100 kpc. This study can be regarded as one of first steps in this mapping endeavor, which is bound to provide unprecedented clues about the formation and evolution of our Galaxy. Indeed, "these are exciting times to study local galaxies" (Wyse 2006).

Acknowledgments

Ž. Ivezić and B. Sesar acknowledge support by NSF grants AST-615991 and AST-0707901, and by NSF grant AST-0551161 to LSST for design and development activity. J. Dalcanton acknowledges NSF CAREER grant AST-02-38683. C. Allende Prieto acknowledges support by NASA grants NAG5-13057 and NAG5-13147. T.C. Beers, Y.S. Lee, and T. Sivarani acknowledge support from the US National Science Foundation under grants AST 04-06784 and AST 07-07776, as well as from grant PHY 02-16783; Physics Frontier Center/Joint Institute for Nuclear Astrophysics (JINA). Funding for the SDSS and SDSS-II has been provided by the Alfred P. Sloan Foundation, the Participating Institutions, the National Science Foundation, the U.S. Department of Energy, the National Aeronautics and Space Administration, the Japanese Monbukagakusho, the Max Planck Society, and the Higher Education Funding Council for England. The SDSS Web Site is http://www.sdss.org/.

The SDSS is managed by the Astrophysical Research Consortium for the Participating Institutions. The Participating Institutions are the American Museum of Natural History, Astrophysical Institute Potsdam, University of Basel, University of Cambridge, Case Western

[21]At the bright end, LSST color errors will be <0.01 mag. An error of 0.01 mag in the $g - r$ color corresponds to a 50 K random error in effective temperature, and an error of 0.01 mag in the $u - g$ color corresponds to a random metallicity error of 0.01 dex at $[Fe/H] = -0.5$ and 0.05 dex at $[Fe/H] = -1.5$.

[22]The 200 million stars from the "metallicity" sample will be observed over 250 times in the g and r bands with signal-to-noise ratios of about 20 or larger per observation even at the faint end (and the final error in the $g-r$ color below 1%). The total number of stars that will be detected by LSST is of the order 10 billion.

Reserve University, University of Chicago, Drexel University, Fermilab, the Institute for Advanced Study, the Japan Participation Group, Johns Hopkins University, the Joint Institute for Nuclear Astrophysics, the Kavli Institute for Particle Astrophysics and Cosmology, the Korean Scientist Group, the Chinese Academy of Sciences (LAMOST), Los Alamos National Laboratory, the Max-Planck-Institute for Astronomy (MPIA), the Max-Planck-Institute for Astrophysics (MPA), New Mexico State University, Ohio State University, University of Pittsburgh, University of Portsmouth, Princeton University, the United States Naval Observatory, and the University of Washington.

Appendix A. Additional Discussion of the Photometric Temperature Estimator

Often the inverse of the effective temperature is fit as a linear function of color (e.g. CPF). The best-fit

$$\frac{5040\,\mathrm{K}}{T_{\rm eff}} = 0.532(g-r) + 0.654 \quad (1)$$

results in the same systematic errors and rms scatter as eq. 3, with the largest difference between the two relations below 50 K.

A lower limit for errors in photometric effective temperature can be readily computed using eq. 3 and photometric errors in the $g-r$ color (the median value is 0.025 mag, and 0.03 mag at $g = 19.5$; these values, computed by photometric pipeline, are reliable, as discussed in detail by Sesar et al. 2007). This is a lower limit because the contribution of errors in spectroscopic effective temperature is not included. The standard deviation for the distribution of metallicity residuals normalized by these errors is 1.2. Hence, one is tempted to conclude that the accuracy of the effective temperature estimator is limited by SDSS photometric errors. However, this conclusion is not consistent with the behavior of the $\log(T_{\rm eff})$ vs. $g-r$ relation for a subset of 13,719 stars for which more accurate photometry, based on ∼10 repeated SDSS observations, is available (Ivezić et al. 2007). Although for these stars the median error in the $g-r$ color is only 0.008 mag, the standard deviation for $\log(T_{\rm eff})$ residuals is not appreciably smaller (the expectation is a decrease by a factor of three). Therefore, it is quite likely that the contribution of errors in spectroscopic effective temperature to the scatter of $\log(T_{\rm eff})$ residuals is not negligible. Indeed, the implied value of ∼100 K agrees well with an independent estimate based on a comparison to high-resolution spectral data, as discussed by Beers at al. 2006. The analyzed color range spans about 15 MK spectral subtypes (from ∼F5 to ∼G9/K0, Bailer-Jones et al. 1997, 1998). Hence, the uncertainty in photometric effective temperature estimate of 100 K corresponds to about one spectral subtype, or equivalently, *an error of one spectral subtype corresponds to a* $g-r$ *error of 0.02 mag.*

A good correlation between spectroscopic effective temperature and $g-r$ color extends beyond the restricted color range where photometric metallicity method is applicable ($0.2 < g-r < 0.4$). We find that everywhere in the $-0.3 < g-r < 1.3$ color range (roughly $-0.1 < B-V < 1.3$), the relation

$$\log(T_{\rm eff}/\mathrm{K}) = 3.882 - 0.316(g-r) + 0.0488(g-r)^2 + 0.0283(g-r)^3 \quad (2)$$

achieves systematic errors below 0.004 dex and overall rms of 0.008 dex. The corresponding temperature range is 4,000 – 10,000 K. When the residuals are binned in 0.1 dex wide bins of metallicity and log(g), the largest median residual is 0.006 dex. Eq. 1 remains valid in the

$-0.3 < g-r < 0.8$ range, but also requires non-linear terms if extended to redder colors (or a different linear fit for the $0.8 < g-r < 1.3$ range).

Due to expanded $g-r$ range, the impact of metallicity and log(g) on log($T_{\rm eff}$) residuals is expected to be larger for this relation than for eq. 3. Using Kurucz (1979) models, we find that the strongest dependence on metallicity is expected in the $0.4 < g-r < 1.2$ color range, with a gradient of ∼0.015 dex/dex (see also Lenz et al. 1998 for a related discussion). The measured value for SDSS sample is 0.012 dex/dex, and implies up to ∼200 K offsets as metallicity varies from −2.0 to −0.5. The strongest dependence on log(g) is expected in the $-0.2 < g-r < 0.1$ color range, with a gradient of 0.02 dex/dex. The measured value for SDSS sample is ∼0.004 dex/dex, or about five times smaller (150 K vs. 720 K variation, as log(g) varies by 2 dex at $g-r=0$). We do not understand the cause of this discrepancy.

Appendix B. Additional Discussion of the Photometric Metallicity Estimator

In two *restricted* color regions, simpler expressions than eq. 4 suffice. In a low-metallicity region defined by $0.8 < u-g < 1.0$ (and $0.2 < g-r < 0.6$, of course), the relation

$$[Fe/H]_{ph} = 5.14(u-g) - 6.10 \quad (1)$$

reproduces the spectroscopic metallicity of about 27,000 stars with an rms scatter of 0.29 dex. We note that this is essentially the same expression as obtained by Ivezić et al. (2006b) using a preliminary version of spectroscopic parameter pipeline, *except for an overall shift in metallicity by 0.2 dex.* This shift is due to the fact that SDSS stellar parameters pipeline was still under development when the analysis of Ivezić et al. (2006b) was performed.

In a high effective temperature region (5800 K $< T_{\rm eff} <$ 6600 K) defined by $0.2 < g-r < 0.4$, the relation

$$[Fe/H]_{ph} = -21.88 + 47.39(u-g) - 35.50(u-g)^2 + 9.018(u-g)^3 \quad (2)$$

reproduces spectroscopic metallicity of about 34,000 stars with an rms scatter of 0.30 dex. In the range $0.8 < u-g < 1.4$ (corresponding to $-2.0 < [Fe/H] < -0.4$) systematic errors do not exceed 0.1 dex. The systematic errors are larger than for eq. 4 because the lines of constant metallicity in the $g-r$ vs. $u-g$ diagram are not exactly vertical. Despite somewhat poorer performance, eqs. 1 and 2 are convenient when estimating the impact of $u-g$ color error on photometric metallicity error. An error in the $u-g$ color of 0.02 mag (typical of both systematic calibration errors and random errors at the bright end for SDSS data) induces an error in $[Fe/H]$ that varies from 0.02 dex at $[Fe/H] = -0.5$ ($u-g$=1.28) to 0.11 dex at $[Fe/H] = -1.5$ ($u-g$=0.89). At $g = 19.5$, the median $u-g$ error for single-epoch SDSS data is 0.06 mag for point sources with $0.2 < g-r < 0.4$, corresponding to median

random metallicity errors of 0.10 dex for disk stars and 0.30 dex for halo stars (for a detailed dependence of SDSS random photometric errors on magnitude, see Sesar et al. 2007).

The metallicity vs. $u-g$ relation has a smaller slope at the red end (both eq. 4 and eq. 2) and effectively introduces an upper limit on estimated metallicity. For example, for $u-g$=1.3 and $g-r=0.4$, $[Fe/H]_{ph}=-0.44$ (from eq. 4, and -0.46 using eq. 2). Such an upper limit is in agreement with the data analyzed here, but we emphasize that the data set does *not* include stars with higher metallicity. Such stars are presumably nearby thin disk stars, and in the $0.2<g-r<0.6$ range are typically saturated in SDSS data (most SDSS data to date are obtained at high galactic latitudes). It is thus possible that metallicity estimates given by both eq. 4 and eq. 2 would be biased towards lower values for stars with $[Fe/H]>-0.5$, resulting in a "metallicity compression". Some evidence that this is a detectable, but not a major effect is discussed in § 3.4.1, and in more detail by Lee et al. (2007b). It will be possible to quantify this effect in detail using the data for metal-rich stars from the ongoing SDSS spectroscopic survey of low Galactic latitudes (SEGUE).

Given that the u band photometric errors limit the precision of photometric metallicity estimates at the faint end, it is prudent to test whether the position of a star in the $r-i$ vs. $g-r$ color-color diagram could be used as an alternative method. We selected subsamples of stars in 0.02 mag wide $g-r$ bins and inspected the dependence of spectroscopic metallicity on the $r-i$ color in the range $-2.5<[Fe/H]<-0.5$. The strongest correlation between $[Fe/H]$ and $r-i$ color is observed around $g-r\sim0.4$, with a gradient of $\Delta(r-i)/\Delta[Fe/H]\sim0.017$ mag/dex. Hence, the effect of metallicity on the $r-i$ color is about 10 times smaller than for the $u-g$ color. With the $r-i$ color kept fixed, we find $\Delta(g-r)/\Delta[Fe/H]\sim0.04$ mag/dex. When using only the gri bands, the photometric metallicity errors are about 0.3 dex at the bright end and 0.5 dex at $g=19.5$ (<0.1 dex and <0.3 dex for ugr based estimates). Therefore, the best approach for estimating photometric metallicity using SDSS data is to use the ugr bands.

REFERENCES

Abadi, M.G., Navarro, J.F., Steinmetz, M. & Eke, V.R. 2003, ApJ, 597, 21

Abazajian, K., Adelman, J.K., Agüeros, M., et al. 2003, AJ, 126, 2081

Abazajian, K., Adelman, J.K., Agüeros, M., et al. 2004, AJ, 129, 1755

Abazajian, K., Adelman, J.K., Agüeros, M., et al. 2005, AJ, 128, 502

Adelman-McCarthy, J.K., Agüeros, M.A., Allam, S.S., et al. 2006, ApJS, 162, 38

Allende Prieto, C., Barklem, P.S., Lambert, D.L. & Cunha, K. 2004, A&A, 420, 183

Allende Prieto, C., Beers, T.C., Wilhelm, R. et al. 2006, ApJ. 636, 804

Allende Prieto, C., Sivarani, T., Beers, T.C., et al. 2007, submitted to AJ

Bahcall, J.N. & Soneira, R.M. 1980, ApJSS, 44, 73

Bailer-Jones, C.A.L., Irwin, M., Gilmore, G. & von Hippel, T. 1997, MNRAS, 292, 157

Bailer-Jones, C.A.L., Irwin, M. & von Hippel, T. 1998, MNRAS, 298, 361

Becker, A.C., Silvestri, N.M., Owen, R.E., Ivezić, Ž., & Lupton, R.H. 2007, submitted to PASP

Beers, T.C., Drilling, J.S., Rossi, S., et al. 2002, AJ, 124, 931

Beers, T.C. & Christlieb, N. 2005, ARA&A, 43, 531

Beers, T.C., Lee, Y., Sivarani, T., et al. 2006, Mem.S.A.It., 77, 1171

Belokurov, V., Zucker, D.B., Evans, N.W., et al. 2006, ApJ, 642, L137

Belokurov, V., Evans, N.W., Irwin, M.J., et al. 2007, ApJ, 658, 337

Bensby, T., Feltzing, S. & Lundström, I. 2003, A&A, 410, 527

Bell, E.F., Zucker, D.B., Belokurov, V. et al. 2007, submitted to ApJ (also astro-ph/0706.0004)

Brook, C.B., Kawata, D., Gibson, B.K. & Freeman, K.C. 2004, ApJ, 612, 894

Bullock, J.S. & Johnston, K.V. 2005, ApJ, 635, 931

Carney, B.W. 1979, ApJ, 233, 211

Carollo, D., Beers, T.C., Lee, Y.S., et al. 2007, accepted by Nature

Casagrande, L., Portinari, L. & Flynn, C. 2006, MNRAS, 373, 13

Chiba, M. & Beers, T.C. 2000, AJ, 119, 2843

Conn, B.C., Martin, N.F., Lewis, G.F., et al. 2005, MNRAS, 364, L13

Covey, K., Ivezić, Ž., Schlegel, D., et al. 2007, accepted to AJ (also astro-ph/0707.4473)

Dehnen, W. & Binney, J.J. 1998, MNRAS, 298, 387

Du, C., Zhou, X., Ma, J., Shi, J., Chen, A.B., Jiang, Z.& Chen, J. 2004, AJ, 128, 2265

Duffau, S., Zinn, R. & Vivas, A.K. 2006, ApJ, 636, L97

Eggen, O.J., Lynden-Bell, D. & Sandage, A.R. 1962, ApJ, 136, 748

Eisenstein, D.J., Annis, J., Gunn, J.E., et al. 2001, AJ, 122, 2267

Eisenstein, D.J., Liebert, J., Harris, H.C., et al. 2006, ApJS, 167, 40

Fan, X. 1999, AJ, 117, 2528

Feltzing, S. 2006, Mem.S.A.It., 77, 1103 (also astro-ph/0611118)

Finlator, K., Ivezić, Ž., Fan, X., et al. 2000, AJ, 120, 2615

Flaugher, B. & Dark Energy Survey Collaboration, 2007, BAAS, 209, 22.01

Freeman, K. & Bland-Hawthorn, J. 2002, ARA&A, 40, 487

Fuhrmann, K. 2004, AN, 325, 3

Fukugita, M., Ichikawa, T., Gunn, J.E., Doi, M., Shimasaku, K., & Schneider, D.P. 1996, AJ, 111, 1748

Gilmore, G. & Reid, N. 1983, MNRAS, 202, 1025

Gilmore, G. & Wyse, R.F.G. 1985, AJ, 90, 2015

Gilmore, G., Wyse, R.F.G., Jones, J.B. 1995, AJ, 109, 1095

Gilmore, G., Wyse, R.F.G. & Kuijken, K. 1989, Annual review of astronomy and astrophysics. Volume 27, pp. 555-627.

Gilmore, G., Wyse, R.F.G., Norris, J.E. 2002, ApJ, 574, L39

Girard, T.M., Korchagin, V.I., Caseti-Dinescu, D.I., van Altena, W.F., López, C.E. & Monet, D.G. 2006, AJ, 132, 1768

Girardi, L. & Salaris, M. 2001, MNRAS, 323, 109

Grillmair, C.J. 2006a, ApJ, 645, L37

Grillmair, C.J. 2006b, ApJ, 651, L29

Gunn, J.E., Knapp, G.R. & Tremaine, S.D. 1979, AJ, 84, 1181

Gunn, J.E., Carr, M., Rockosi, C., et al. 1998, AJ, 116, 3040

Gunn, J.E., Siegmund, W.A., Mannery, E.J., et al. 2006, AJ, 131, 2332

Helmi, A., Ivezić, Ž., Prada, F., et al. 2003, ApJ, 586, 195

Helmi, A., White, S.D.M., de Zeeuw, P.T. & Zhao, H. 1999, Nature, 402, 53

Hogg, D.W., Finkbeiner, D.P., Schlegel, D.J. & Gunn, J.E. 2002, AJ, 122, 2129

Holberg, J.B. & Bergeron, P. 2006, AJ, 132, 1221

Ivezić, Ž., Goldston, J., Finlator, K., et al. 2000, AJ, 120, 963

Ivezić, Ž., Lupton, R.H., Anderson, S., et al. 2003, Proceedings of the Workshop *Variability with Wide Field Imagers*, Mem. Soc. Ast. It., 74, 978 (also astro-ph/0301400)

Ivezić, Ž., Lupton, R.H., Schlegel, D., et al. 2004, AN, 325, 583

Ivezić, Ž., Bond, N., Jurić, M., et al. 2005, ASP Conference Series, Vol. 338, Proceedings of a meeting held 18-20 October 2004 at Lowell Observatory, Flagstaff, Arizona, USA. Edited by P. Kenneth Seidelmann and Alice K. B. Monet. San Francisco: Astronomical Society of the Pacific, 2005., p.201 (also astro-ph/0701502)

Ivezić, Ž., Smith, J. A., Miknaitis, G., et al. 2006a, astro-ph/0701508

Ivezić, Ž., Schlegel, D., Uomoto, A., et al. 2006b, Mem. Soc. Ast. It., 77, 1057

Ivezić, Ž., Smith, J. A., Miknaitis, G., et al. 2007, AJ, 134, 973

Jackson, T., Ivezić, Ž. & Knapp, G.R. 2002, MNRAS, 337, 749

Jurić, M., Ivezić, Ž., Brooks, A., et al. 2008, accepted to ApJ, (also astro-ph/0510520) (J08)

Jorgensen, B.R. & Lindegren, L. 2005, A&A, 436, 127

Kaiser, N., Aussel, It., Burke, B.E., et al. 2002, in "Survey and Other Telescope Technologies and Discoveries", Tyson, J.A. & Wolff, S., eds. Proceedings of the SPIE, 4836, 154

Karaali, S., Bilir, S. & Tuncel, S. 2005, PASA, 22, 24

Keller, S.C., Schmidt, B.P., Bessell, M.S., et al. 2007, astro-ph/0702511

Kurucz, R.L. 1979, ApJS, 40, 1

Laird, J.B., Carney, B.W. & Latham, D.W. 1988, AJ, 95, 1843

Lee, Y.S., Beers, T.C., Sivarani, T., et al. 2007a, submitted to AJ

Lee, Y.S., Beers, T.C., Sivarani, T., et al. 2007b, submitted to AJ

Lenz, D.D., Newberg, J., Rosner, R., Richards, G.T., Stoughton, C. 1998, ApJS, 119, 121

Lupton, R.H. 1993, *Statistics in Theory and Practice*, Princeton University Press, Princeton, New Jersey

Lupton, R.H., Ivezić, Ž., Gunn, J.E., Knapp, G.R., Strauss, M.A. & Yasuda, N. 2002, in "Survey and Other Telescope Technologies and Discoveries", Tyson, J.A. & Wolff, S., eds. Proceedings of the SPIE, 4836, 350

Majewski, S.R. 1992, ApJS, 78, 87

Majewski, S.R. 1993, ARA&A, 31, 575

Majewski, S.R., Skrutskie, M.F., Weinberg, M.D. & Ostheimer, J.C. 2003, ApJ, 599, 1082

Mannery, E.J. & Wallerstein, G. 1971, AJ, 76, 9

Martin, N.F., Irwin, M.J., Ibata, R.A., et al. 2006, MNRAS, 367, L69

Morrison, H.L., Flynn, C. & Freeman, K.C. 1990, 100, 1191

Munn, J.A., Monet, D.G., Levine, S.E., et al. 2004, AJ, 127, 3034

Newberg H.J., Yanny, B., Rockosi, C., et al. 2002, ApJ, 569, 245

Nordström, B., Mayor, M., Andersen, J., et al. 2004, A&A, 418, 989

Norris, J. 1987, ApJ, 314, L39

Ojha, D.K., Bienayme, O., Robin, A.C., Creze, M. & Mohan, V. 1996, A&A, 311, 456

Pagel, B.E.J. & Patchett, B.E. 1975, MNRAS, 172, 13

Penarrubia, J., Martinez-Delgado, D., Rix, H.W., et al. 2005, ApJ, 626, 128

Perryman, M.A.C., de Boer, K.S., Gilmore, G., et al. 2001; A&A, 369, 339

Pickles, A.J. 1998, PASP, 110, 863

Pier, J.R., Munn, J.A., Hindsley, R.B., Hennesy, G.S., Kent, S.M., Lupton, R.H. & Ivezić, Ž. 2003, AJ, 125, 1559

Pourbaix, D., Knapp, G.R., Szkody, P., et al. 2005, A&A, 444, 643

Ramírez, I. & Meléndez, J. 2005, ApJ, 626, 465

Ramírez, I., Allende Prieto, C. & Lambert, D.L. 2007, A&A, 465, 271

Reddy, B.E., Lambert, D.L. & Allende Prieto, C. 2006, MNRAS, 367, 1329

Reid, I.N., van Wyk, F., Marang, F., et al. 2001, MNRAS, 325, 931

Reid, I.N., Gizis, J.E. & Hawley, S.L. 2002, AJ, 124, 2721

Richards, G., Fan, X., Newberg, H., et al. 2002, AJ, 123, 2945

Robin, A.C., Reylé, C., Derriére, S. & Picaud, S. 2003, A&A, 409, 523

Ryan, S.G. & Norris, J.E. 1991, AJ, 101, 1835

Sandage, A. 1969, ApJ, 158, 1115

Sandage, A. & Smith, L.L. 1963, ApJ, 137, 1057

Schlegel, D., Finkbeiner,D.P. & Davis, M. 1998, ApJ500, 525

Schneider, D. P., Hall, P. B., Richards, G. T. et al. 2007, accepted to AJ

Schwarzschild, M., Searle, L. & Howard, R. 1955, ApJ, 122, 353

Scranton, R., Johnston, D., et al. 2002, ApJ, 579, 48

Sesar, B., Ivezić, Ž., Lupton, R.H., et al. 2007, accepted to AJ (also astro-ph/0704.0655)

Sekiguchi, M. & Fukugita, M. 2000, AJ, 120, 1072

Siegel, M.H., Majewski, S.R., Reid, I.N., & Thompson, I.B. 2002, ApJ, 578, 151

Skrutskie, M.F., Cutri, R.M., Stiening, R., et al. 2006, AJ, 131, 1163

Smith, J.A., Tucker, D.L., Kent, S.M., et al. 2002, AJ, 123, 2121

Smolčić, V., Ivezić, Ž., Knapp, G.R., et al. 2004, ApJ, 615, L141

Snider, S., Allende Prieto, C., von Hippel, T. Beers, T.C., Sneden, C., Qu, Y. & Rossi, S. 2001, ApJ, 562, 528

Springel, V. & Hernquist, L. 2003, MNRAS, 339, 312

Stoughton, C., Lupton, R.H., Bernardi, M., et al. 2002, AJ, 123, 485

Strauss, M.A., Weinberg, D.H., Lupton, R.H., et al. 2002, AJ 124, 1810

Strömgren, B. 1966, ARA&A, 4, 433

Tinsley, B.M. 1975, ApJ, 197, 159

Tucker, D., Kent, S., Richmond, M.W., et al. 2006, AN, 327, 821

Tyson, J.A. 2002, in *Survey and Other Telescope Technologies and Discoveries*, Tyson, J.A. & Wolff, S., eds. Proceedings of the SPIE, 4836, 10

Vivas, A.K., Zinn, R., Andrews, P., *et al.* 2001, ApJ, 554, L33

Vivas, A.K. & Zinn, R. 2006, AJ, 132, 714

Wallerstein, G. 1962, ApJS, 6, 407

Weinberg, M.D. 1992, ApJ, 384, 81

Wilkinson, M.I., Vallenari, A., Turon, C., et al. 2005, MNRAS, 359, 1306

Wyse, R.F.G. & Gilmore, G. 1995, AJ, 110, 2771

Wyse, R.F.G. 2006, Mem.S.A.It., 77, 1036

Yanny, B., Newberg, H. J., Kent, S., et al. 2000, ApJ, 540, 825

York, D.G., Adelman, J., Anderson, S., et al. 2000, AJ, 120, 1579

This preprint was prepared with the AAS LaTeX macros v5.2.

Table 1. The sample distance limits

$(g-r)$	$(r-i)^a$	M_g^b	D^c	$(B-V)^d$	M_V^e
0.2	0.03	3.79	13.9	0.35	3.65
0.3	0.08	4.42	10.4	0.46	4.23
0.4	0.12	5.00	7.9	0.57	4.77
0.5	0.16	5.54	6.2	0.68	5.26
0.6	0.20	6.05	4.9	0.77	5.71
0.7	0.24	6.52	3.9	0.86	6.12
0.8	0.28	6.97	3.2	0.95	6.52
0.9	0.32	7.40	2.6	1.04	6.88
1.0	0.37	7.81	2.2	1.12	7.23
1.1	0.42	8.20	1.8	1.21	7.57
1.2	0.48	8.65	1.5	1.29	7.96

[a]The mean $r-i$ color on the main stellar locus for the $g-r$ color listed in first column, evaluated using eq. 2.

[b]The absolute magnitude in the g band, evaluated using eq. 1.

[c]The distance for a star with $g = 19.5$ (kpc).

[d]The Johnson $B-V$ color, computed for convenience from SDSS photometry using transformations from Ivezić et al. (2006).

[e]The absolute magnitude in the Johnson V band, computed from M_g.

Table 2. The best-fit parameters for Gaussians shown in Fig. 4

g range[a]	N[b]	μ[c]	σ[d]	μ error[d]
15.0–15.5	1087	1.095	0.078	2.4
15.5–16.0	1605	1.085	0.076	1.9
16.0–16.5	1911	1.082	0.070	1.6
16.5–17.0	2328	1.078	0.070	1.5
17.0–17.5	2590	1.075	0.064	1.3
18.0–18.5	3348	0.899	0.050	0.9
18.5–19.0	3745	0.901	0.055	0.9
19.0–19.5	4504	0.895	0.055	0.8
19.5–20.0	5893	0.891	0.060	0.8
20.0–20.5	8712	0.886	0.075	0.8

[a]The g magnitude range.

[b]The number of stars in bin.

[c]The best-fit mean $u - g$ color (only data with $u - g > 1.0$ are fit in the five brightest bins, and data with $u - g < 0.95$ in the five faintest bins (see Figure 4).

[d]The best-fit distribution width.

[e]The statistical error in the mean (milimag).

Table 3. Best-fit parameters for $p([Fe/H]|Z)$ shown in Fig. 7

$\|Z\|$ range[a]	$\langle\|Z\|\rangle$[b]	N[c]	f_H^d	f_H^e	f_H^f	μ_H^g	σ_H^h
0.8–1.0	0.89	2,876	0.07	0.09	0.06	-1.38	0.27
1.5–2.0	1.72	3,339	0.24	0.22	0.20	-1.38	0.27
3.0–4.0	3.46	2,315	0.71	0.60	0.61	-1.38	0.27
5.0–7.0	5.76	4,820	0.97	0.90	0.90	-1.46	0.30

[a]The $|Z|$ range for each bin (kpc).

[b]The median $|Z|$ in each bin (kpc).

[c]The number of stars in the corresponding bin.

[d]The halo-to-disk number ratio predicted by the J08 best-fit model (see § 3.3.4).

[e]The halo-to-disk number ratio predicted by eq. 8.

[f]The best-fit halo-to-disk number ratio. The halo parameters are only weakly constrained in the first bin.

[g]The best-fit mean metallicity for the halo component.

[h]The best-fit distribution width for the halo component.

Table 4. Best-fit parameters for $p(v_\Phi)$ shown in Fig. 11

Z range[a]	$\langle Z \rangle$[b]	N[c]	$\langle g \rangle$[d]	v_{d1}^e	v_{d2}^f	σ_{d1}^g	σ_{d2}^h	f_H^i	σ_H^j	σ_v^k
0.5–1.0	0.89	945	14.6	11	56	22	44	0.09	101	13
1.5–2.0	1.74	3,321	16.0	28	73	31	49	0.23	103	25
3.0–4.0	3.48	5,334	17.4	61	106	53	65	0.61	112	50
5.0–7.0	6.01	9,950	18.5	109	154	88	96	0.91	132	85

[a]The Z range for bin (kpc).

[b]The median Z in bin (kpc).

[c]The number of stars in bin.

[d]The median g band magnitude in bin.

[e]The mean velocity for the first Gaussian disk component, computed using eq. 14 (km/s).

[f]The mean velocity for the second Gaussian disk component, $v_{d2} = v_{d1} + 45$, (km/s).

[g]The velocity dispersion for the first Gaussian disk component convolved with measurement errors (km/s).

[h]The velocity dispersion for the second Gaussian disk component convolved with measurement errors (km/s).

[i]The halo-to-disk number ratio computed using eq 8.

[j]The velocity dispersion for halo component convolved with measurement errors (km/s).

[k]An estimate for the velocity measurement error (median for all stars in the bin, km/s).

Table 5. Best-fit parameters for $p(v_\Phi)$ shown in Fig. 13

Z range[a]	$\langle Z \rangle$[b]	N[c]	$\langle g \rangle$[d]	σ^e_{d1}	σ^f_{d2}	σ^g_H	f^h_H	r^i_{DD}	r^j_{DD}
0.5–1.0	0.89	945	14.6	23	32	111	4	0.7	1.5
1.0–1.3	1.14	1,379	15.1	23	32	111	11	1.0	2.6
1.5–2.0	1.74	3,321	16.0	31	38	113	16	3.9	15

[a]The Z range for bin (kpc).

[b]The median Z in bin (kpc).

[c]The number of stars in bin.

[d]The median g band magnitude in bin.

[e]The velocity dispersion for the first Gaussian disk component convolved with measurement errors (km/s).

[f]The velocity dispersion for the second Gaussian disk component convolved with measurement errors (km/s).

[g]The velocity dispersion for the halo component convolved with measurement errors(km/s).

[h]The best-fit fraction of halo stars (%).

[i]The best-fit thick-to-thin disk star number ratio.

[j]The thick-to-thin disk star number ratio predicted using J08 model (see § 3.3.4).

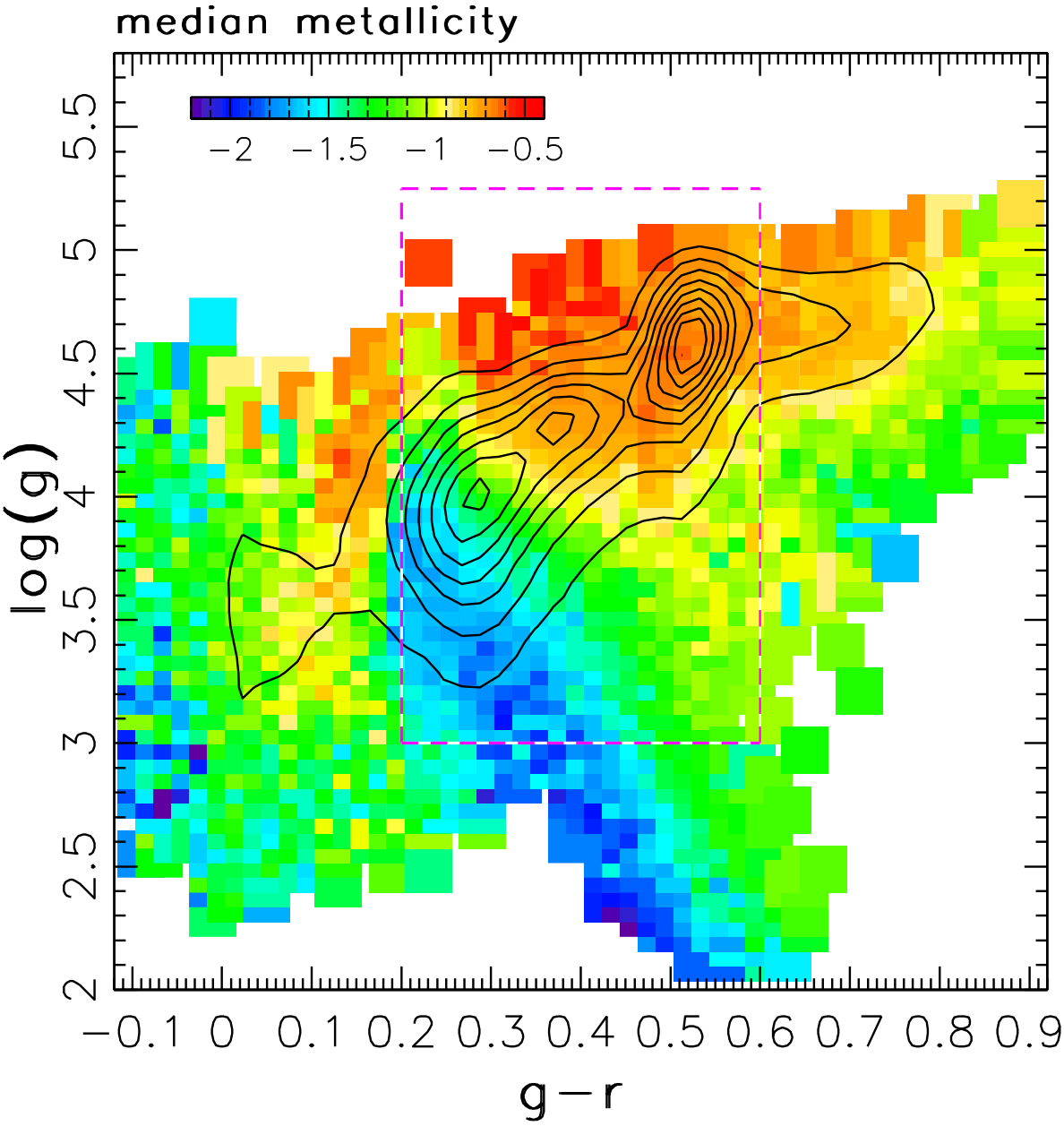

Fig. 1.— The linearly-spaced contours show the distribution of ∼110,000 stars with $g < 19.5$ and $-0.1 < g - r < 0.9$ (corresponding to effective temperature in the 4500 K to 8200 K range) from the SDSS DR6 spectroscopic sample in the log(g) vs. $g - r$ plane. The tri-modal distribution is a result of SDSS target selection algorithm. The color scheme shows the median metallicity in all 0.02 mag by 0.06 dex large pixels that contain at least 10 stars. The fraction of stars with log(g)<3 (giants) is 4%, and they are mostly found in two color regions: $-0.1 < g - r < 0.2$ (BHB stars) and $0.4 < g - r < 0.65$ (red giants). They are dominated by low-metallicity stars ($[Fe/H] < -1$). The dashed lines outline the region selected for deriving photometric estimates for effective temperature and metallicity.

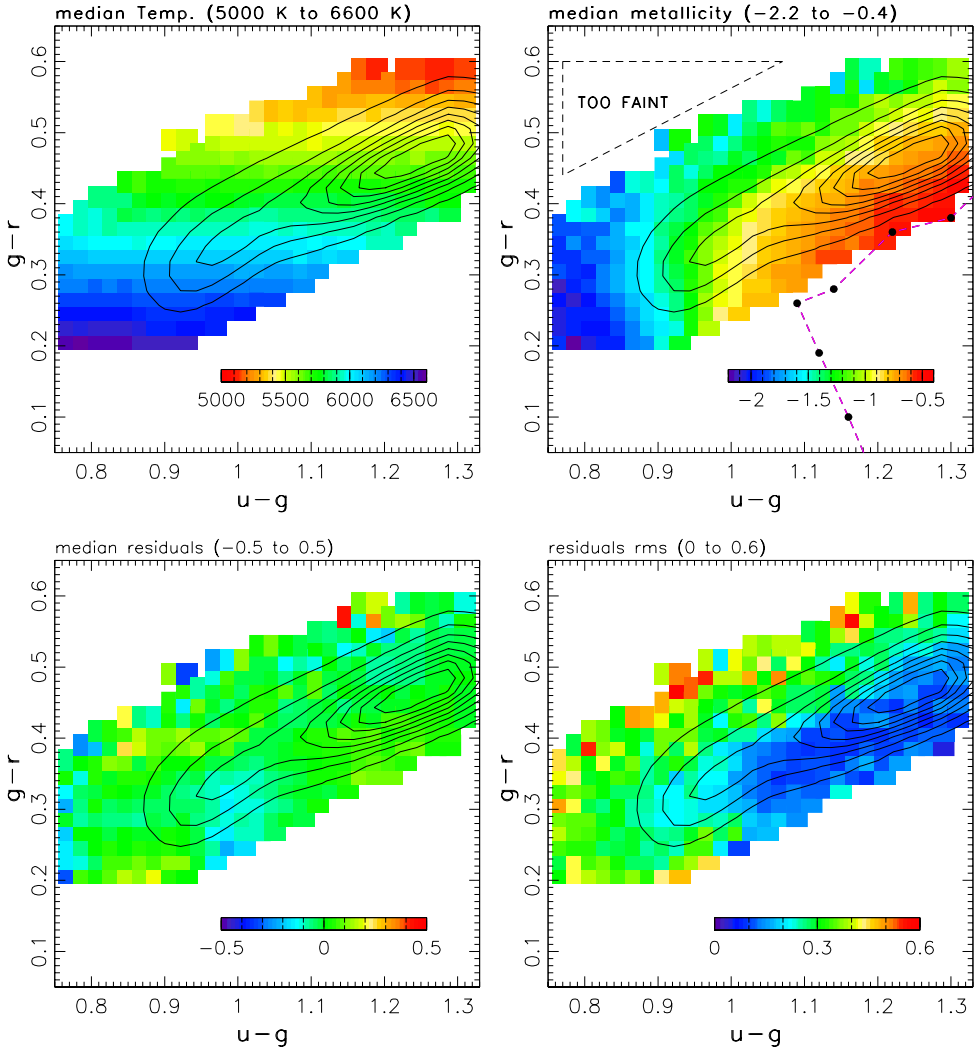

Fig. 2.— The correlation of spectroscopic effective temperature (top left) and metallicity (top right) with the position of a star in the $g-r$ vs. $u-g$ color-color diagram. The color scheme shows the median values in all 0.02 mag by 0.02 mag large pixels that contain at least 10 stars. The distribution of stars in an *imaging* sample with $g < 19.5$ is shown by linearly-spaced contours. The dots show the synthetic colors for the Pickles (1998) solar metallicity standards (F0, F2, F5, F6, F8, and G0, from bottom to top), taken from Covey et al. (2007). The triangular region marked "TOO FAINT" in the top right panel contains no stars due to $g < 19.5$ flux limit and the fact that low-metallicity stars are generally more distant and fainter than high-metallicity stars. The bottom left panel shows the median residuals between spectroscopic metallicity and photometric estimates based on eq. 4. Their root-mean-square scatter (over all pixels) is 0.06 dex. The bottom right panel shows a map of the root-mean scatter of metallicity for individual stars in each pixel. Its median value is 0.21 dex. The scatter is larger for weak-lines low-metallicity stars (∼0.3 dex) than for high-metallicity stars (∼0.15 dex).

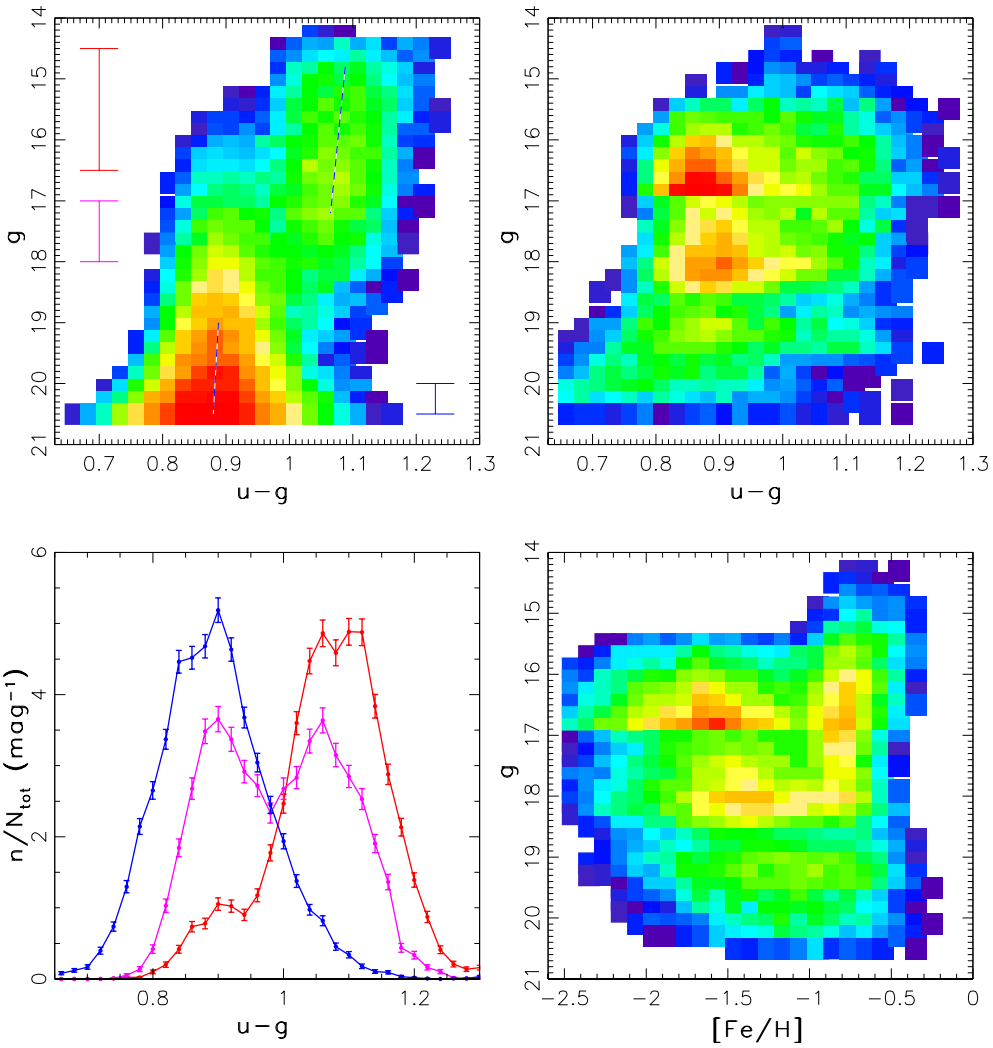

Fig. 3.— The top left panel shows the distribution of stars (logarithm of counts in each bin) from the SDSS Stripe 82 catalog with $0.2 < g - r < 0.4$ in the g vs. $u - g$ color-magnitude diagram. In this $g - r$ range, the $u - g$ color is a proxy for metallicity (see eq. 2 in Appendix B). The two concentrations of stars correspond to disk ($u - g \sim 1.1$) and halo ($u - g \sim 0.9$) stars, with the dashed lines indicating the change of the median $u - g$ color with magnitude for each concentration. The $u - g$ color distributions in three magnitude slices, marked by vertical bars in the top left panel, are shown in the bottom left panel. All three histograms can be approximately described by a sum of two ∼0.07 mag wide Gaussians centered on $u - g$=0.90 and 1.08, with the number ratio of blue to red component increasing with magnitude from 1:7 to 20:1. For detailed fits to the $u - g$ color distribution as a function of magnitude, see Figure 4. The top right panel is analogous to the top left panel, except that a complete imaging sample of stars is replaced by stars from the SDSS spectroscopic survey. The spectroscopic sample is highly incomplete, as evident from the patchy distribution. The bottom right panel shows the same sample of stars from the spectroscopic survey, with the $u - g$ color replaced by spectroscopic metallicity.

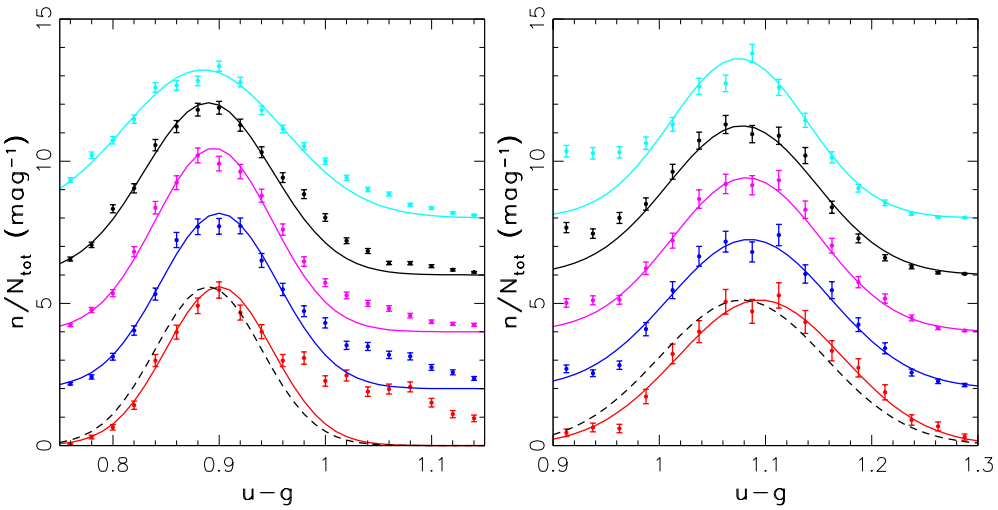

Fig. 4.— The symbols with error bars show the $u-g$ color distributions in 0.5 mag wide magnitude slices (see the top left panel in Figure 3), in the range $g = 18 - 20.5$ (left) and $g = 14.5 - 17.0$ (right). The bottom histograms correspond to the brightest bin, and each histogram is successively offset by 2 for clarity. The solid lines show the best-fit Gaussians, fit to data with $u-g < 0.95$ (left) and $u-g > 1.0$ (right), to minimize contamination by disk and halo stars, respectively. The best-fit parameters are listed in Table 2. The dashed black lines are the same as the solid black lines, and are added to illustrate the shift of histograms towards bluer colors for the faint bins. The gradients of the $u-g$ color with respect to the g magnitude are -0.006 ± 0.002 mag/mag (left) and -0.012 ± 0.002 mag/mag (right).

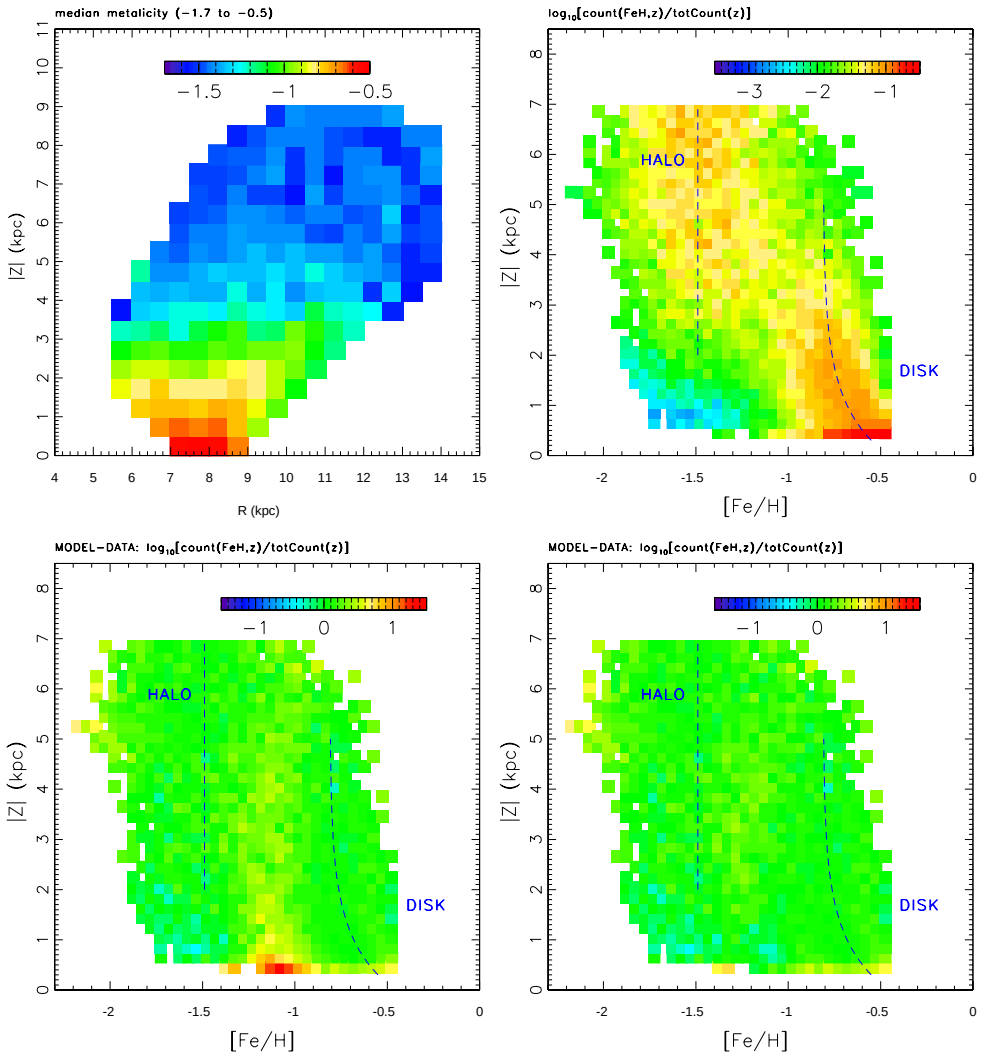

Fig. 5.— The top left panel illustrates the dependence of the median photometric metallicity for ∼76,000 stars from SDSS stripe 82 coadded photometric catalog with $14 < g < 20.5$, $0.2 < g - r < 0.4$ and photometric distance in the 0.5–10 kpc range, on cylindrical galactic coordinates R and Z. Note that the Z gradient is much larger than the R gradient (∼0.1 dex/kpc vs. <0.01 dex/kpc). The top right panel shows the conditional metallicity probability distribution at a given distance from the Galactic plane for ∼28,000 stars with $7 < R/\mathrm{kpc} < 9$ (the probability density is shown on a logarithmic scale, with its integral normalized to 1). The two concentrations of stars correspond to disk ($[Fe/H] \sim -0.7$) and halo ($[Fe/H] \sim -1.5$) stars. The difference between this map and a two-component Gaussian model described in § 3.3 is shown in the bottom left panel with the same dynamic range for color coding as used in the top right panel. The residual feature visible around $[Fe/H] \sim -1.1$ and $Z \sim 1$ kpc can be modeled either as a third Gaussian component, or by adopting non-Gaussian metallicity distribution for the disk component. The residuals map for the former is shown in the bottom right panel.

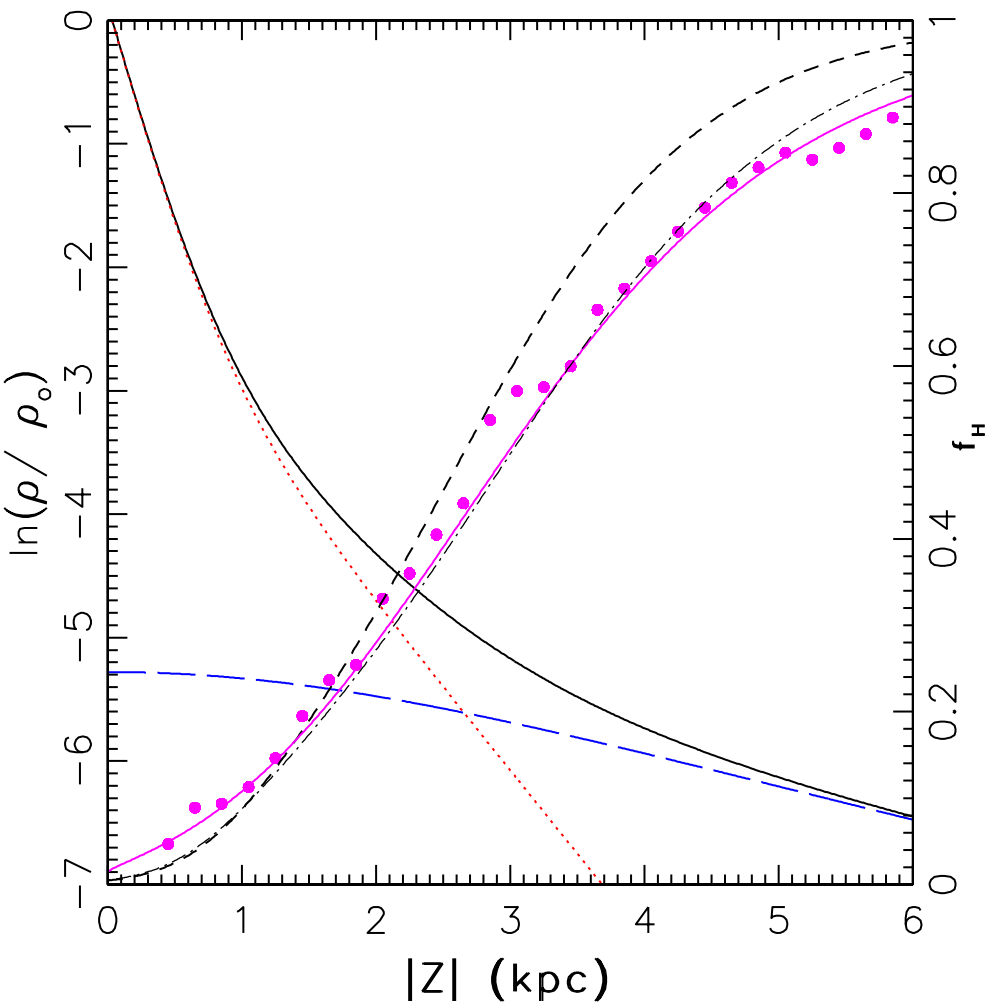

Fig. 6.— The symbols show the number ratio of stars with $[Fe/H] < -1$ and those with $[Fe/H] > -1$, for stars with 7 kpc $< R <$ 9 kpc (with the ratio labeled on the right y axis). Beyond $Z = 3$ kpc, metal-poor stars dominate the counts. The solid line passing through the symbols is a three-parameter best fit used in modeling the conditional metallicity probability distribution (equal to $1/(1+70\eta)$, with $\eta = \exp(-|Z/300\mathrm{pc}|^{0.63})$). The short-dashed line is a prediction for the halo-to-disk counts ratio based on a best-fit Galaxy model to stellar counts from Jurić et al. (2008). The model includes an oblate power-law halo, and exponential thin and thick disks (see § 3.3.4). The disk contribution to counts is shown by the dotted line (with the ln(counts) labeled on the left y axis), and the long-dashed line shows the halo contribution. The sum of disk and halo contributions is shown by the solid line. The dot-dashed line is the halo-to-disk counts ratio for a modified Jurić et al. model (see text).

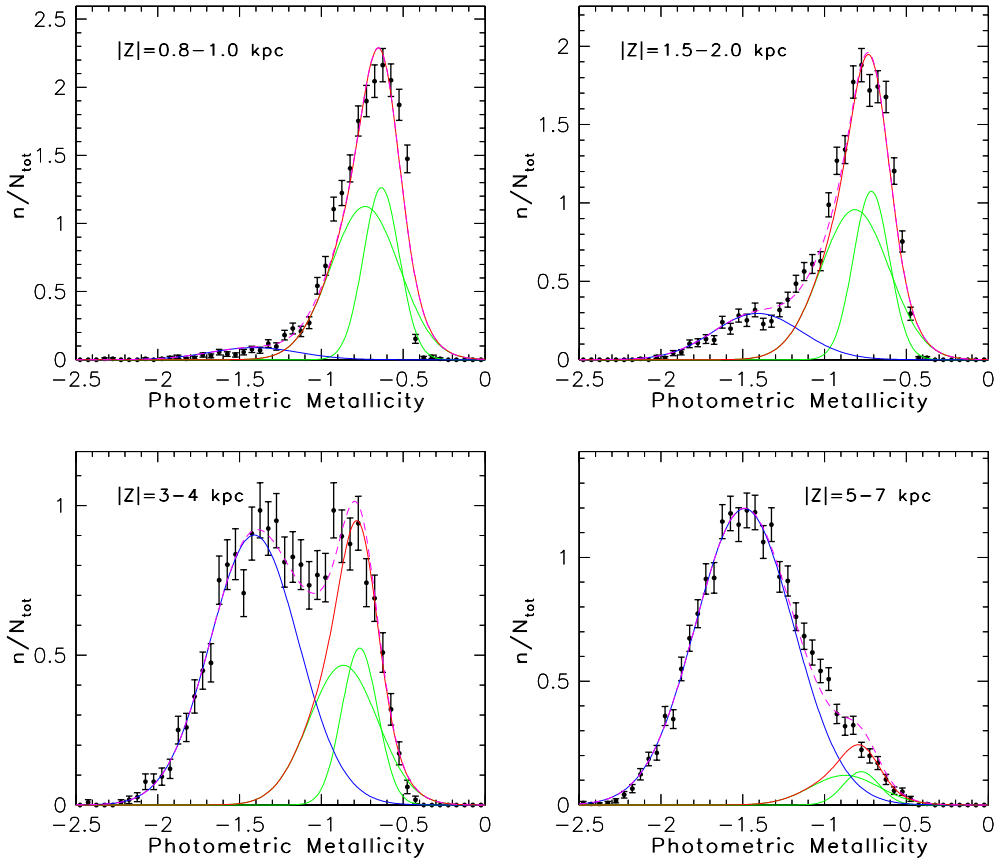

Fig. 7.— The symbols with error bars show measured photometric metallicity distribution for stars with $0.2 < g - r < 0.4$, 7 kpc $< R <$ 9 kpc and the distance from the galactic plane in the range 0.8–1.0 kpc (top left, ∼2,900 stars), 1.5–2.0 kpc (top right, ∼3,300 stars), 3.0–4.0 kpc (bottom left, ∼2,300 stars) and 5.0–7.0 kpc (bottom right, ∼4,800 stars). The histograms are essentially horizontal (parallel to x axis) slices at corresponding $|Z|$ intervals through the map shown in the top right panel in Figure 5. The dashed magenta lines show a best-fit two-component, halo plus disk, model. The blue lines show the halo contribution, modeled as a single Gaussian, and the red lines show the contribution of a non-Gaussian disk model, modeled as a sum of two Gaussians shown by the green lines. See § 3.3.1 and Table 3 for best-fit parameters.

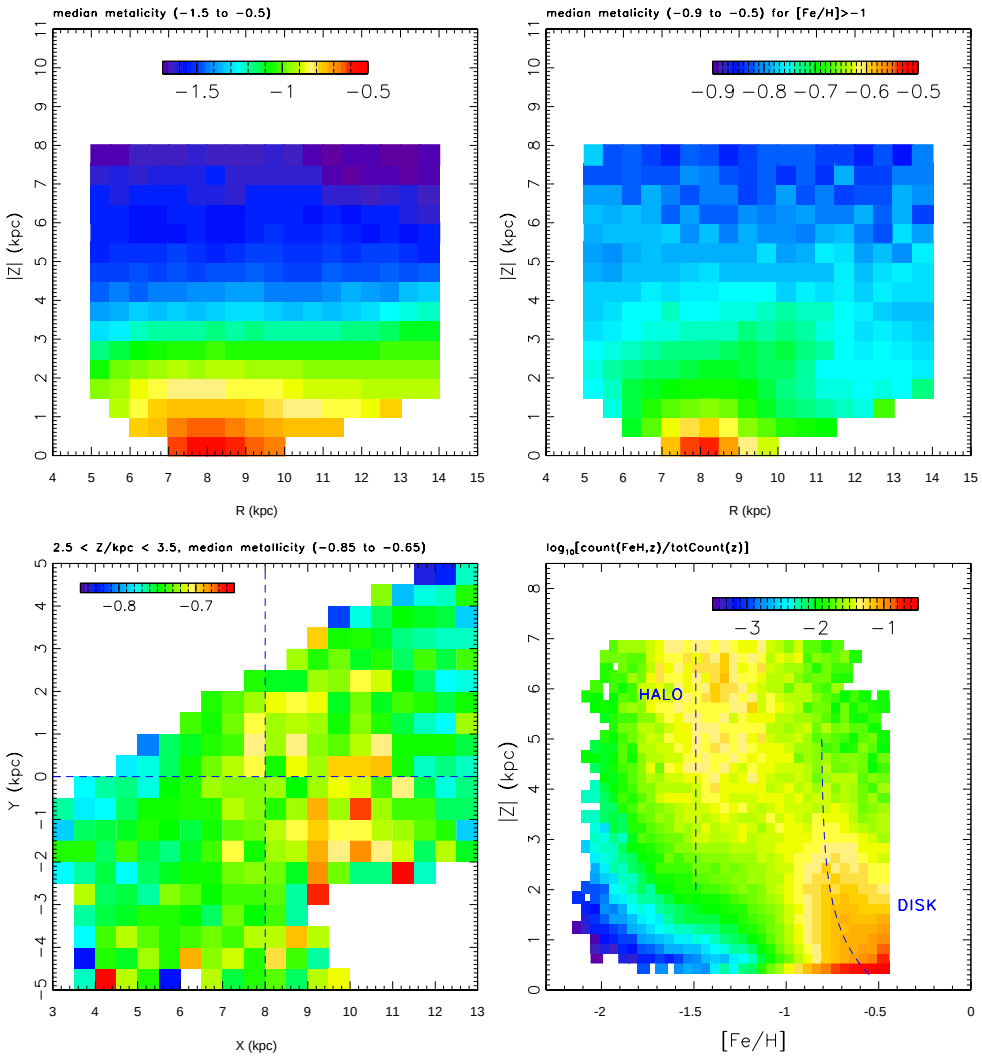

Fig. 8.— The top left panel illustrates the dependence of the median photometric metallicity for ∼2.1 million stars from SDSS Data Release 6 with $14 < g < 19.5$, $0.2 < g - r < 0.4$ and photometric distance in the 0.5–10 kpc range, on cylindrical galactic coordinates R and Z (compare to the top left panel in Figure 5). The top right panel is analogous, except that only high-metallicity stars with $[Fe/H] > -1.0$ are used, and display stretch is harder, as indicated in the panel. Note a coherent feature at $R \sim 10$ kpc and $Z \sim 3$ kpc. Its extent parallel to the Galactic plane is shown in the bottom left panel, which shows the median metallicity for stars with $2.5 < Z/\mathrm{kpc} < 3.5$ (note the much harder display stretch). The bottom right panel shows the conditional metallicity probability distribution for ∼300,000 stars from a cylinder perpendicular to the Galactic plane, centered on the Sun, and with a radius of 1 kpc. The dashed lines are the same fiducials as shown in the top right panel in Figure 5.

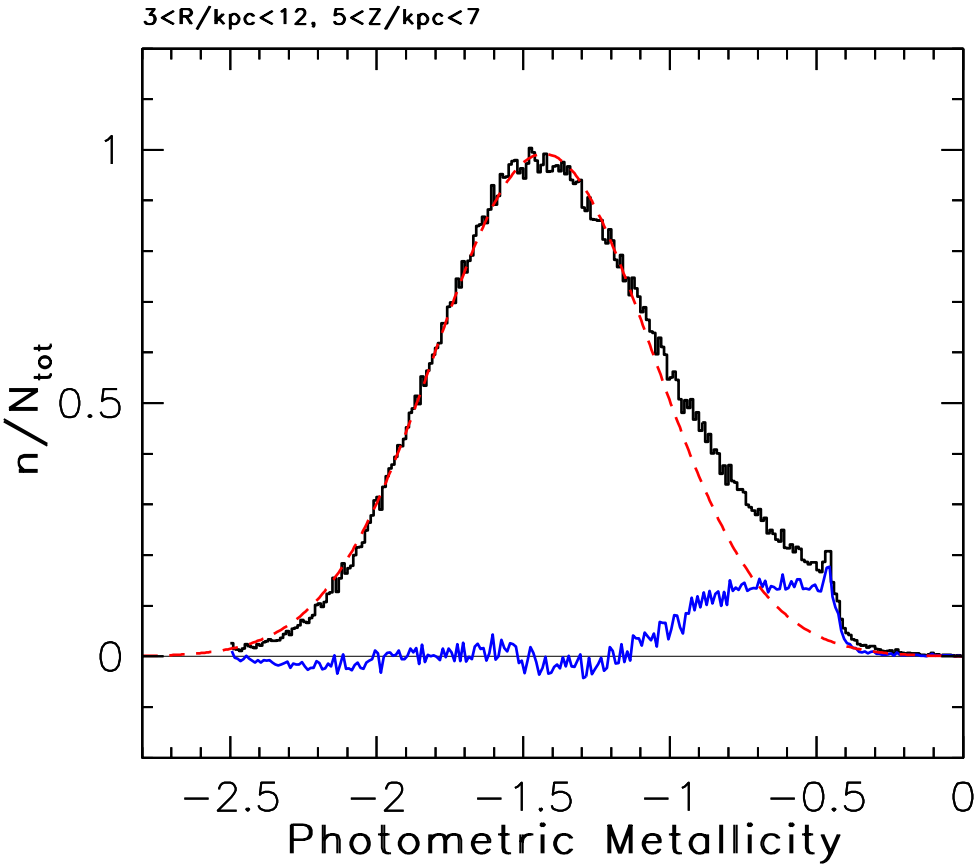

Fig. 9.— The black histogram shows photometric metallicity distribution for ∼259,000 stars with $3 < R/\mathrm{kpc} < 12$ and $5 < Z/\mathrm{kpc} < 7$ (compare to the bottom right panel in Figure 7). The dashed red line is a Gaussian with a width of 0.37 dex, centered on $[Fe/H] = -1.43$, and an area of 0.92. The difference between the observed distribution and this Gaussian is shown by the blue line, and presumably corresponds to disk stars. The small peak around $[Fe/H] = -0.5$ is probably an artifact of photometric metallicity estimation method.

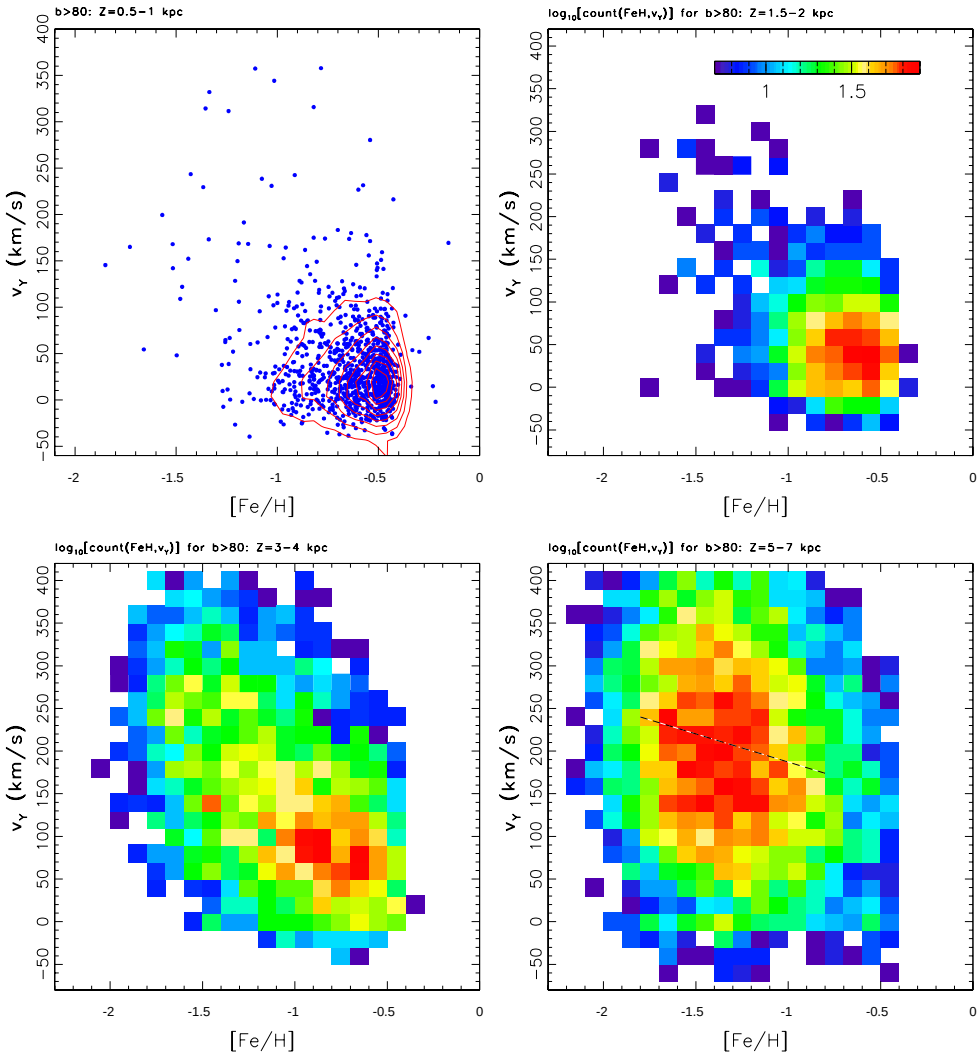

Fig. 10.— The distribution of stars observed towards the north Galactic pole ($|b| > 80°$) in the velocity-metallicity diagrams, and as a function of distance from the plane in the range 0.5–1.0 kpc (top left, ∼960 stars), 1.5–2.0 kpc (top right, ∼3,400 stars), 3.0–4.0 kpc (bottom left, ∼5,400 stars) and 5.0–7.0 kpc (bottom right, ∼10,000 stars). In the top left panel, individual stars are shown by symbols and the distribution is emphasized by linearly spaced contours. In other three panels, the maps show the logarithm of counts in each bin, according to the legend shown in the top right panel. Towards the north galactic pole, the plotted velocity component (v_Y) corresponds to rotational component. Its median value for subsamples selected by $[Fe/H] > -1$ in the top right panel is 48 km/s and 96 km/s in the bottom left panel. The median value for subsamples selected by $[Fe/H] < -1$ is 192 km/s and 215 km/s, respectively. For marginal v_Y distributions, see Figure 11. The dashed line in the bottom right panel corresponds to eq. 15 (see § 3.4.5).

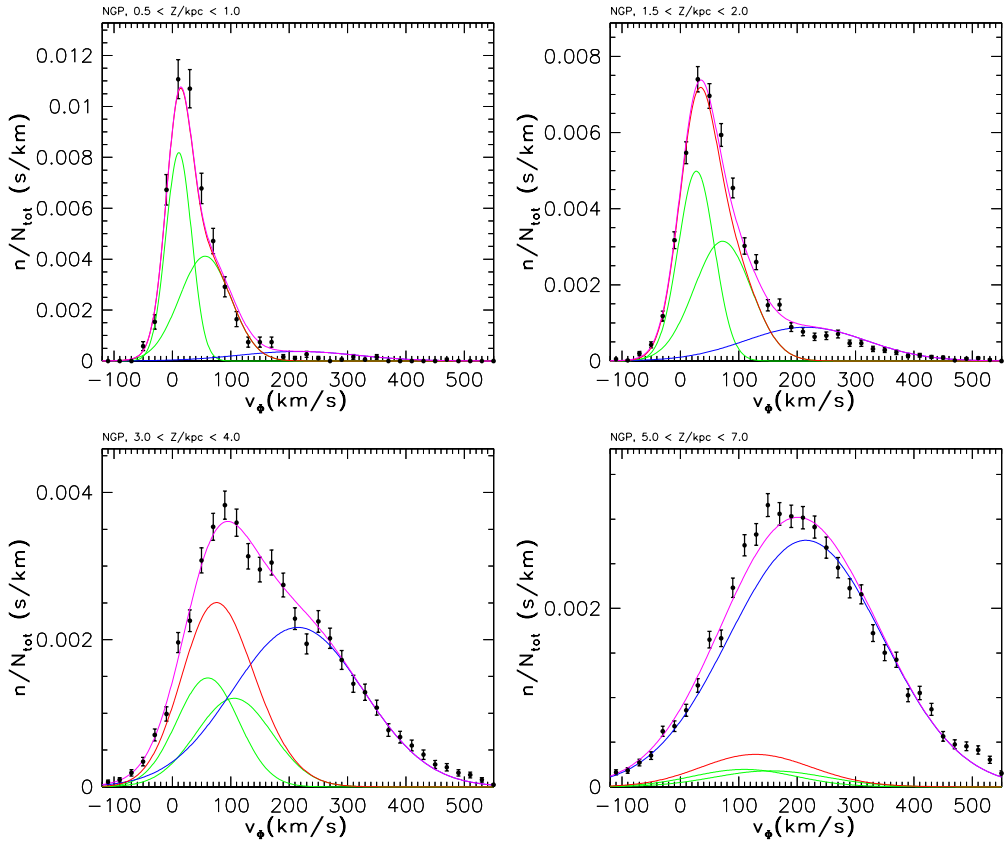

Fig. 11.— The symbols with error bars show measured rotational velocity distribution for stars with $0.2 < g - r < 0.4$, $b > 80°$, and the distance from the galactic plane in the range 0.5–1.0 kpc (top left, ∼950 stars), 1.5–2.0 kpc (top right, ∼3,300 stars), 3.0–4.0 kpc (bottom left, ∼5,300 stars) and 5.0–7.0 kpc (bottom right, ∼10,000 stars). These histograms are marginal v_Y distributions for the maps shown in Figure 10. The red curves show the contribution of a non-Gaussian disk model (a sum of two Gaussians, shown as green lines), the blue curves show halo contribution, and the magenta curves are their sum (see § 3.4.3 for details and Table 4 for best-fit parameters).

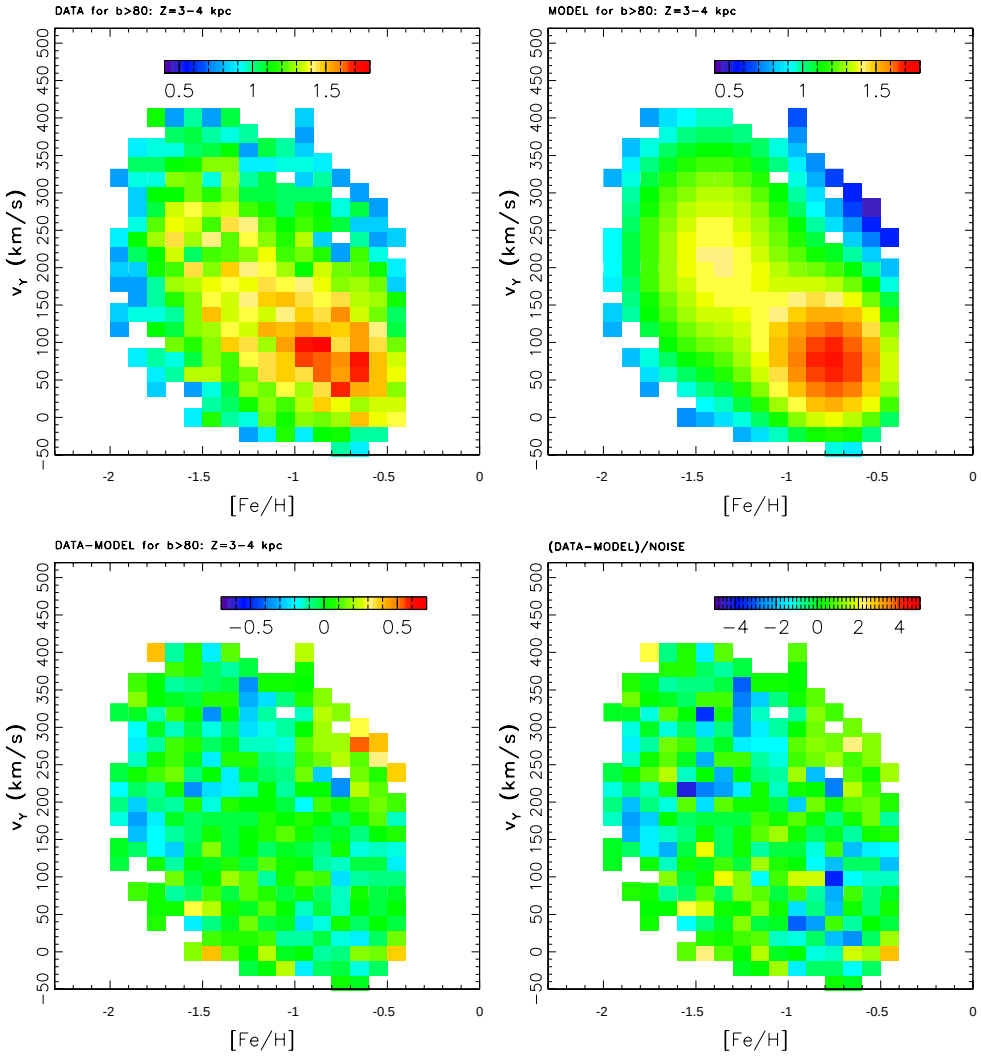

Fig. 12.— The top left panel shows distribution of stars (logarithm of counts in each bin) observed towards the north Galactic pole ($|b| > 80°$), and with $3.0 < Z/\mathrm{kpc} < 4$ kpc, in the velocity-metallicity diagram (same map as in the bottom left panel in Figure 10). The top right panel shows a best-fit model assuming that velocity and metallicity distributions are uncorrelated, when disk and halo components are treated separately, and are given by the best fits shown in the bottom left panel of Figure 7 for metallicity distribution, and in the bottom left panel of Figure 11 for velocity distribution. The bottom left panel shows the logarithm of (data/model) ratio, displayed with the same dynamic range as the top two panels. The observed counts are predicted with an rms scatter of 33%. This scatter is consistent with expected statistical noise. The bottom right panel shows the data-model difference map normalized by the expected noise. The rms width of the distribution is 1.09.

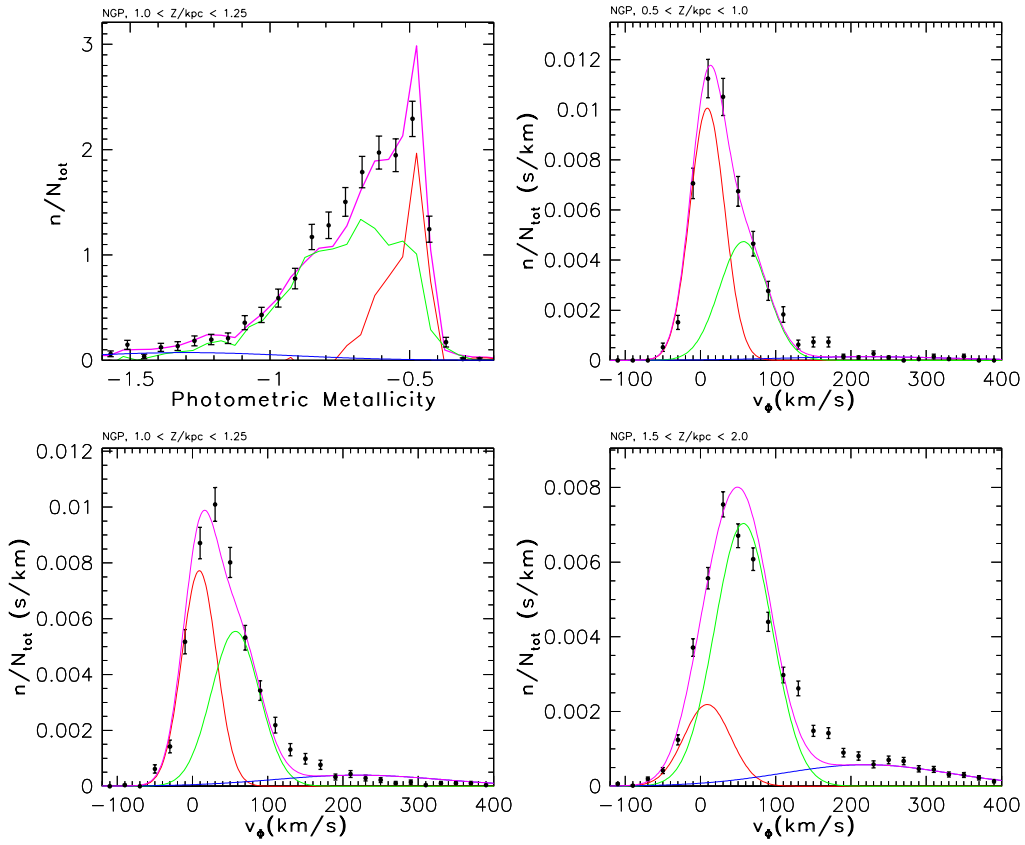

Fig. 13.— The top left panel illustrates a test of the hypothesis that the observed variation of metallicity distribution with Z is due to a varying mixing ratio of the independent thin and thick disk metallicity distributions. The latter are determined using metallicity distributions in the $|Z| = 0.5 - 1.0$ kpc and $|Z| = 2.0 - 2.5$ kpc bins, and are shown as red (thin disk) and green (thick disk) lines, scaled using the 2.6:1 thick-to-thin disk number ratio expected for the displayed $|Z| = 1.0 - 1.25$ kpc bin from the counts profile. The blue line shows halo contribution (11%), and the magenta line is the sum of these three components. The data are shown by symbols with error bars. The remaining three panels show measured rotational velocity distributions in three Z slices (symbols with error bars; 0.5-1 kpc: top left; 1.0-1.25 kpc: bottom right; 1.5-2.0 kpc: bottom right). The blue curves are Gaussians corresponding to halo stars, with the parameters listed in Table 5. The red lines are Gaussians centered on 9 km/s, and the green lines are Gaussians centered on 57 km/s, with widths listed in Table 5. The increase of their widths with Z is consistent with estimated measurement errors; the implied intrinsic widths are 18 km/s for narrow Gaussians, and 28 km/s for wide Gaussians. These curves are normalized according to thick-to-thin number ratio and halo contribution listed in Table 5.

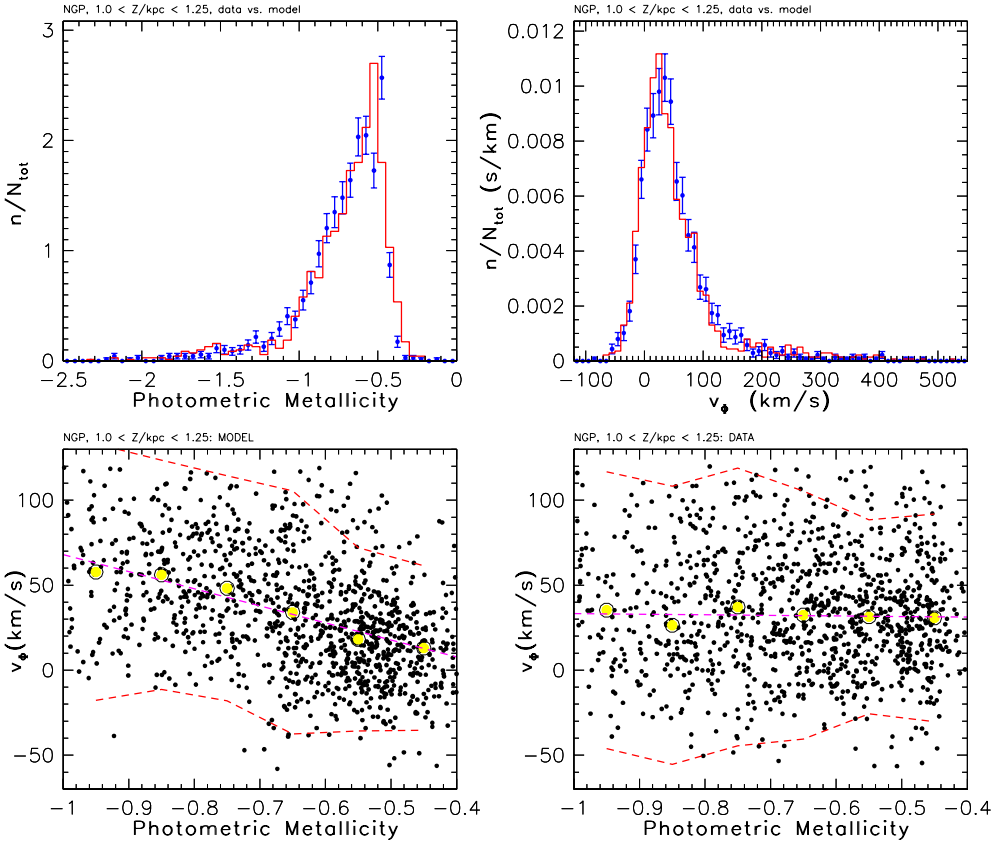

Fig. 14.— A comparison of data for 1379 stars with $b > 80$ and $1.0 < Z/\mathrm{kpc} < 1.25$ kpc, and a model based on a traditional disk decomposition into thin and thick components. The model assumes three Gaussians with equal contributions of thin and thick disk stars, and halo stars contributing 11%. The Gaussians describing metallicity distribution (top left panel, symbols represent data and histogram represents model) are centered on $[Fe/H] = -0.52, -0.77$ and -1.37, and have widths of 0.06, 0.13, and 0.32 dex, with a measurement error contribution of 0.07 dex added in quadrature. The Gaussians describing velocity distribution (top right panel) are centered on 9, 57 and 220 km/s, and have widths of 18, 28, and 100 km/s, with a measurement error contribution of 16 km/s added in quadrature. The two bottom panels show the two-dimensional distributions in the velocity-metallicity diagram for model (left) and data (right), with individual stars shown as small dots. The large dots show the median velocity in 0.1 dex wide metallicity bins, for stars with velocity in the −60 km/s to 120 km/s range. The 2-σ envelope around these medians is shown as two outer dashed lines. The dashed lines in the middle show the best linear fit to the median velocity, with slopes of −101 km/s/dex (model) and −2.0 km/s/dex (data).

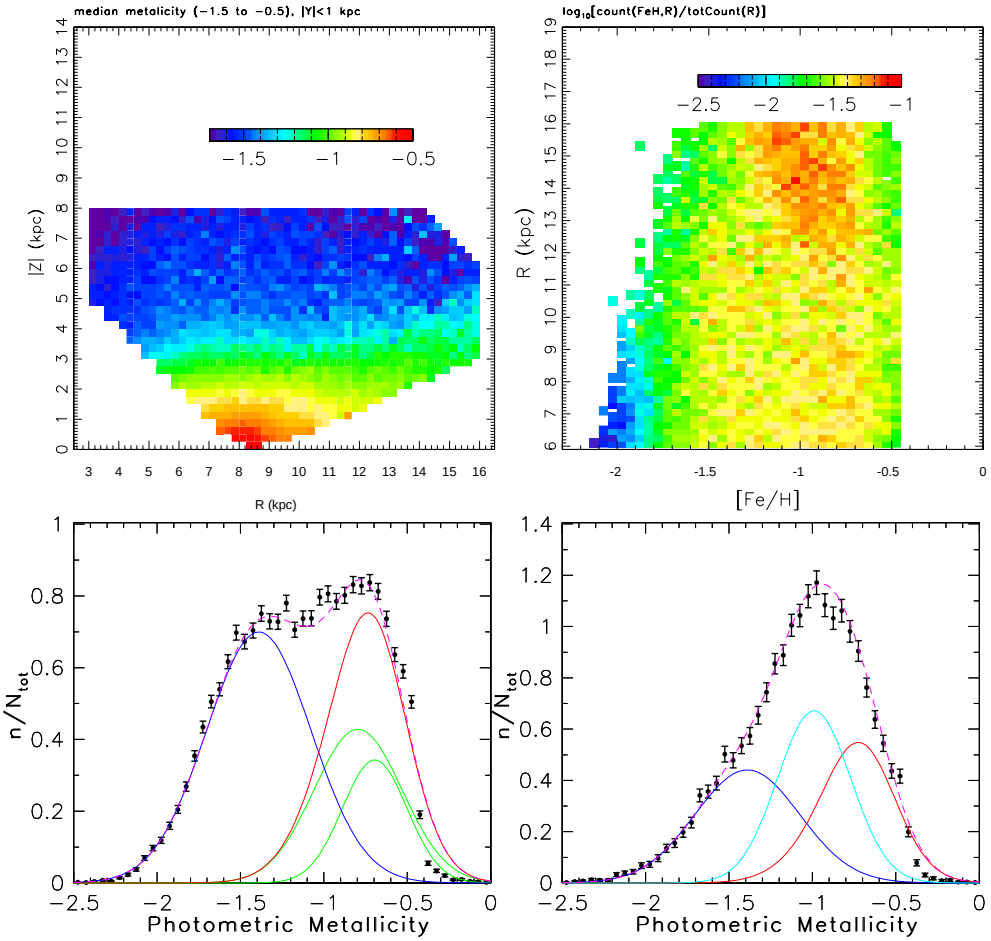

Fig. 15.— The top left panel illustrates the dependence of the median photometric metallicity for ∼0.97 million stars from SDSS Data Release 6 with $14 < g < 19.5$, $0.2 < g - r < 0.4$ and $|Y| < 1$ kpc, on cylindrical galactic coordinates R and Z. This Y range is selected to include the Monoceros stream, which represents an overdensity by a factor of ∼2 in a region around $R \sim 15$ kpc and Z ∼3–4 kpc. As discernible from the map, this region has a larger median metallicity than expected for this Z range from smaller R. The top right panel shows the conditional metallicity probability distribution for a subsample of ∼93,000 stars with $3 < Z/\mathrm{kpc} < 4$. The strong overdensity at $R > 12$ kpc is the Monoceros stream. The bottom panels show the metallicity distribution (symbols with error bars) for a subsample of ∼33,000 stars with $6 < R/\mathrm{kpc} < 9$ (left) and for ∼11,000 stars with $13 < R/\mathrm{kpc} < 16$. The curves have the same meaning as in Figure 7, with the addition of the cyan curve in the right panel. This curve is a 0.22 dex wide Gaussian centered on $[Fe/H] = -0.96$, and accounts for 37% stars in the sample that presumably belong to the Monoceros stream (see § 3.5.1 for details).

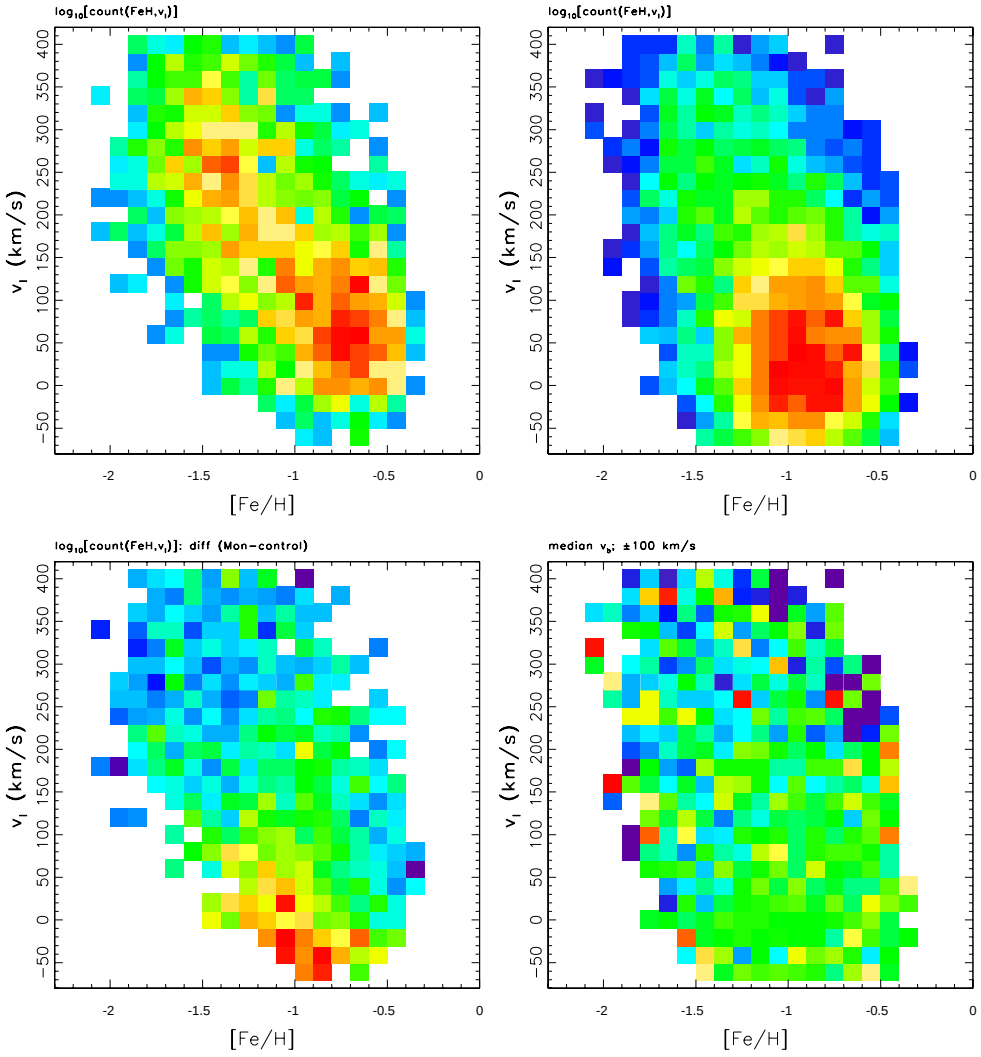

Fig. 16.— The top left panel shows the distribution of ∼6,000 stars (logarithm of counts in each bin) with $|Y| < 1$ kpc, $3 < Z/\mathrm{kpc} < 4$, $9 < R/\mathrm{kpc} < 12$ and $170° < l < 190°$, in the longitudinal velocity vs. photometric metallicity plane (a slice through the map shown in the top right panel in Figure 15). The longitudinal velocity is based on proper motion measurements, and at selected $l \sim 180$ corresponds to rotational component. The top right panel is analogous, except that ∼11,000 stars are selected from the $13 < R/\mathrm{kpc} < 16$ radial range which maximizes the fraction of stars from the Monoceros stream (clustered around $[Fe/H] \sim -1$ and $v_l \sim 25$ km/s. The difference of these two maps is shown in the bottom left panel. The bottom right panel shows the median latitudinal velocity (v_b) for stars in the latter (Monoceros) subsample (±100 km/s stretch, green corresponds to 0 km/s). The analogous map for the $9 < R/\mathrm{kpc} < 12$ subsample looks similar.